J. Fluid Mech. (2011), *vol.* 677, *pp.* 218–254.
doi:10.1017/jfm.2011.78

Fluxes across double-diffusive interfaces: a one-dimensional-turbulence study

ESTEBAN GONZALEZ-JUEZ[1], ALAN R. KERSTEIN[1]† AND DAVID O. LIGNELL[2]

[1]Combustion Research Facility, Sandia National Laboratories, Livermore, CA 94551-0969, USA

[2]Department of Chemical Engineering, Brigham Young University, Provo, UT 84602, USA

(Received 27 July 2010; revised 30 October 2010; accepted 10 February 2011; first published online 12 April 2011)

This work is a parametric study of the fluxes of heat and salt across unsheared and sheared double-diffusive interfaces using one-dimensional-turbulence (ODT) simulations. It is motivated by the need to understand how these fluxes scale with parameters related to the fluid molecular properties and background shear. Comparisons are made throughout with previous models and available measurements. In unsheared interfaces, ODT simulations show that the dimensionless heat flux Nu scales with the stability parameter R_ρ, Rayleigh number Ra and Prandtl number Pr as $Nu \sim (Ra/R_\rho)^{0.37\pm0.03}$ when Pr varies from 3 to 100 and as $Nu \sim (Ra/R_\rho)^{0.31} Pr^{0.22\pm0.04}$ when Pr varies from 0.01 to 1. Here Ra/R_ρ can be seen as the ratio of destabilizing and stabilizing effects. The simulation results also indicate that the ratio of salt and heat fluxes R_f is independent of Pr, scales with the Lewis number Le as $R_f \sim Le^{0.41\pm0.04}$ when R_ρ is large enough and deviates from this expression for low values of R_ρ, when the interface becomes heavily eroded. In sheared interfaces, the simulations show three flow regimes. When the Richardson number $Ri \ll 1$, shear-induced mixing dominates, the heat flux scales with the horizontal velocity difference across the interface and $R_f = R_\rho$. Near $Ri \sim 1$ the heat and salt fluxes are seen to increase abruptly as the shear increases. The flow structure and scaling of the fluxes are similar to those of unsheared interfaces when $Ri \gg 1$.

Key words: double-diffusive convection, turbulent convection, turbulence modelling

1. Introduction

1.1. *Background*

Double-diffusive convection occurs in a fluid when two of the fluid components that have opposing effects on the vertical density field, which remains stable on average, have very different molecular diffusivities. The component that is unstably stratified drives the convection, while the stably stratified component hinders it. In the fingering regime of double-diffusive convection the slower diffusing component (salt) is unstably stratified, while in the diffusive regime the component that diffuses faster (temperature) is unstably stratified. The present work is a study of the diffusive regime. This regime is also called the oscillatory regime, thermosolutal or thermohaline convection, or semi-convection. This form of convection is characterized by a staircase structure formed by well-mixed convecting layers separated by density interfaces (Turner 1979).

† Email address for correspondence: arkerst@sandia.gov

Such interfaces are called double-diffusive interfaces. Double-diffusive convection in the diffusive regime occurs, for example, in the Arctic and Southern Oceans, in regions where the melting ice releases cold fresh water over denser warm salty water; in geothermally heated salty lakes, where the bottom heating acts against salt stratification; and in solar ponds, where solar energy is stored in an underlying hot brine (cf. Turner 1974). This regime of double diffusion is believed to be important in massive stars (Merryfield 1995; Paparella, Spiegel & Talon 2002) and giant planets (Chabrier & Baraffe 2007). Therefore, knowing the parametric dependence of the fluxes of heat and salt across double-diffusive interfaces could be of importance, for example, to estimate the flux of heat to the surface of the Arctic and Southern Oceans; in the design of solar ponds and to calculate the speed at which massive stars and giant planets evolve. The present work is a study of this parametric dependence.

1.2. *Previous work and present objectives*

Within the framework of the Boussinesq approximation (§ 2), the parametric dependence of the fluxes of heat F_T and salt F_S across double-diffusive interfaces between well-mixed convecting layers of total depth h can be expressed as

$$Nu = F(t^*, R_\rho, Ra, Ri, Pr, Le), \quad R_f = G(t^*, R_\rho, Ra, Ri, Pr, Le), \tag{1.1}$$

where F and G are functions. Throughout this work F_T is termed a heat flux though it is defined by $F_T = H/(\rho_0 c_p)$, where H is the heat flux, ρ_0 is a reference density and c_p is the specific heat. The dimensionless dependent variables are the Nusselt number Nu and the ratio of buoyancy fluxes R_f, which are defined by

$$Nu = \frac{F_T}{\kappa_T \Delta T/h}, \quad R_f = \frac{\beta_S F_S}{\beta_T F_T}, \tag{1.2}$$

where κ_T is the thermal diffusivity, ΔT is the difference in temperature across the interface, and β_T and β_S are, respectively, the coefficients of thermal expansion and salinity contraction. The dimensionless independent variables are a dimensionless time t^*, the stability parameter R_ρ, the Rayleigh number Ra, the Richardson number Ri, the Prandtl number Pr and the Lewis number Le. These are defined by

$$R_\rho = \frac{\beta_S \Delta S}{\beta_T \Delta T}, \quad Ra = \frac{g\beta_T \Delta T h^3}{\nu \kappa_T}, \quad Ri = \frac{g(\Delta\rho/\rho_0)h}{\Delta U^2}, \quad Pr = \frac{\nu}{\kappa_T}, \quad Le = \frac{\kappa_S}{\kappa_T}, \tag{1.3}$$

where ΔS, $\Delta\rho$ and ΔU are, respectively, the salinity, density and velocity steps across the interface; g is the gravitational acceleration; ν is the fluid kinematic viscosity; and κ_S is the salt diffusivity. In addition, Nu and R_f may depend on boundary conditions.

The above parametric dependence has been studied in double-diffusive interfaces with no background shear in various experimental and theoretical investigations, e.g. Turner (1965), Crapper (1975), Marmorino & Caldwell (1976), Linden & Shirtcliffe (1978), Fernando (1989) and Worster (2004). The prototypical experiment is that in which a layer of saline water with overlying fresh water is heated from below in an insulated tank. By assuming quasi-steady-state conditions and a heat flux F_T independent of the layer thickness h, dimensional arguments suggest that (1.1) becomes $Nu/Ra^{1/3} = F(R_\rho)$ and $R_f = G(R_\rho)$ for fixed values of Pr and Le (Turner 1965). Experiments show that $F(R_\rho)$ decreases with increasing R_ρ, as the stratification becomes stronger and slows down the convection. They also show that $G(R_\rho)$ remains approximately constant when R_ρ lies between 2 and $Le^{-1/2}$, in a regime where molecular effects are important, while it increases with decreasing R_ρ as $R_\rho \to 1$,

as turbulent transport dominates (e.g. Turner 1965; Crapper 1975; Marmorino & Caldwell 1976).

Even though the scaling $Nu \sim Ra^{1/3}$ is widely assumed, the only support for it is the experimental work by Marmorino & Caldwell (1976), which reports $Nu \sim Ra^{0.37\pm0.1}$ (cf. Kelley *et al.* 2003). Our first objective is to determine how the fluxes of heat and salt scale with Ra in the range $Ra = 10^6$–10^{10} (§§ 3.3 and 3.4). We will see that our results are close to those obtained via dimensional reasoning.

Apart from the heat/salt system at ambient conditions ($Pr \approx 7$, $Le \approx 0.01$), other systems of interest are, for example, the heat/salt system at Arctic conditions ($Le \approx 0.005$, cf. Kelley *et al.* 2003), and the heat/H–He system in giant planets ($Pr \approx 0.01$–1 and $Le \approx 0.001$–0.1, cf. Chabrier & Baraffe 2007) and stars ($Pr \sim 10^{-5}$ and $Le \sim 10^{-8}$, cf. Merryfield 1995). It is unclear, however, how the fluxes in the well-studied heat/salt system at ambient conditions compare with those in other systems. This is because the dependence of the fluxes on Pr has not been studied and there are contradictory experimental results on how R_f depends on Le (cf. Turner 1965; Shirtcliffe 1973; Takao & Narusawa 1980). Our second objective is, therefore, to explore in more depth than previous studies the dependence of the fluxes on molecular fluid properties, represented by Pr and Le, in the ranges $Pr = 0.01$–100 and $Le = 0.001$–0.1 (§§ 3.5 and 3.6).

In oceanic double-diffusive interfaces the turbulence is usually generated by both the unstably stratified temperature and shear (Crapper 1976). Micro-structure measurements have shown this mixture of double-diffusive convection and shear turbulence (Larson & Gregg 1983; Padman & Dillon 1991; Inoue *et al.* 2007). There are, however, no studies of sheared double-diffusive interfaces under controlled conditions. Only recently has a model been proposed for the study of these interfaces (Canuto, Cheng & Howard 2008*a*). Predictions from this model for the fingering regime agree well with ocean observations, but predictions for the diffusive regime have not yet been compared to other results. Such comparison is important since models like that of Canuto *et al.* (2008*a*) are ultimately used in ocean circulation models. Thus, our third and final objective is to study the effect of background shear on the heat and salt fluxes across double-diffusive interfaces (§ 4). Our results will show a transition near $Ri \sim 1$ between a shear-dominated regime and a double-diffusion-dominated regime. We will also show how the heat and salt fluxes scale in these regimes.

1.3. *Current approach*

To address the above objectives, we conduct one-dimensional-turbulence (ODT) simulations (Kerstein 1999*a*). These objectives are very challenging to address with laboratory experiments and direct numerical simulations (DNS). ODT simulations are fully resolved, unsteady, stochastic simulations that emulate Navier–Stokes turbulence (§ 2). These simulations have two key features. First, the velocity vector and other properties of the flow reside on a one-dimensional (1D) domain, which can be thought of as a line of sight through the three-dimensional (3D) flow field. This 1D formulation allows full resolution of the interaction between the large scales and the molecular transport scales with computationally affordable simulations but restricts its application, in the present context, to horizontally homogeneous flows. Second, because vortical overturns cannot occur on a 1D domain, turbulent advection is represented using a stochastic mapping process. In comparison, while Reynolds-averaged Navier–Stokes simulations and large-eddy simulations model the small-scale phenomena and retain the 3D representation of the flow, ODT resolves all the scales

of motion but models 3D turbulence. Many features of various types of turbulent flows have been captured using ODT (e.g. Kerstein 1999*a*,*b*; Dreeben & Kerstein 2000; Echekki *et al.* 2001; Kerstein *et al.* 2001; Wunsch & Kerstein 2001, 2005; Ashurst & Kerstein 2005; Kerstein & Wunsch 2006). Of relevance to the present work are previous findings showing the ability of ODT to reproduce known scalings in flows where buoyancy is important (Kerstein 1999*a*; Dreeben & Kerstein 2000; Wunsch & Kerstein 2001, 2005).

In the present context, ODT is well suited to study double-diffusive convection in the diffusive regime, which is characterized by a strong coupling between turbulent advection and molecular transport and can be assumed to be horizontally homogeneous. This motivated a previous study of this type of convection with ODT, which demonstrated that ODT simulations capture the formation and evolution of a diffusive staircase as observed in bottom-heated experiments, and predict fluxes of heat and salt consistent with those observed in various experiments (Kerstein 1999*b*).

In summary, the present work is a parametric study of the fluxes of heat and salt across double-diffusive interfaces. We use results from ODT simulations to determine the approximate scaling of these fluxes with the dominant parameters and identify transition regions in the parameter space. While previous studies, including the work by Kerstein (1999*b*), focused on unsheared interfaces within a limited parameter space, we consider a broader parameter space, including the effect of background shear, whose investigation is enabled by the more recent version of ODT described in Kerstein (2009). Next, this version of ODT is discussed in § 2, and results for unsheared and sheared interfaces are presented respectively in §§ 3 and 4.

2. One-dimensional-turbulence model

2.1. *Overview*

The Boussinesq approximation is invoked by assuming the relative density difference ρ/ρ_0 to be negligibly small except in terms multiplied by gravity g. The density ρ is represented with $\rho/\rho_0 = \beta_S S - \beta_T T$, where ρ, T and S are deviations from reference values. The velocity vector $(u_1, u_2, u_3) = (u, v, w)$, as well as ρ, T and S, is defined in a 1D domain along the vertical coordinate z, where $0 \leqslant z \leqslant h$. These flow properties are advanced in time by integrating the following equations representing molecular transport:

$$\frac{\partial u_i}{\partial t} = \nu \frac{\partial^2 u_i}{\partial z^2}, \quad \frac{\partial T}{\partial t} = \kappa_T \frac{\partial^2 T}{\partial z^2}, \quad \frac{\partial S}{\partial t} = \kappa_S \frac{\partial^2 S}{\partial z^2}, \tag{2.1}$$

for $i = 1, 2, 3$, and through a stochastic process representing turbulent advection. This stochastic process consists of a random sequence of vortical overturns or eddy events. The process is specified by defining the operations performed during an eddy event and the sampling of such events, i.e. the rules governing the time scale τ, length scale l and location z_0 of the eddy events. These operations and sampling rules are discussed next.

2.2. *Operations during an eddy event*

An eddy event consists of two operations. One is a triplet mapping of u_i, T and S representing the vertical displacement of fluid elements by a notional eddy. The second is a modification of u_i representing the energy redistribution between velocity components induced by pressure and the effect of buoyancy forces. These operations

are represented symbolically as

$$u_i(z) \to u_i(f(z)) + c_i K(z), \quad T(z) \to T(f(z)), \quad S(z) \to S(f(z)), \tag{2.2}$$

where the (continuous) triplet mapping operation $f(z)$ is defined by

$$f(z) = z_0 + \begin{cases} 3(z - z_0) & \text{if } z_0 \leqslant z \leqslant z_0 + l/3, \\ 2l - 3(z - z_0) & \text{if } z_0 + l/3 \leqslant z \leqslant z_0 + 2l/3, \\ 3(z - z_0) - 2l & \text{if } z_0 + 2l/3 \leqslant z \leqslant z_0 + l, \\ z - z_0 & \text{otherwise,} \end{cases} \tag{2.3}$$

and the addition of $c_i K(z)$ represents velocity changes due to pressure gradients and buoyancy forces. According to this prescription, the fluid at a location $f(z)$ is moved to a location z by the mapping operation, thus defining the map in terms of its inverse $f(z)$.

The effect of the triplet map on a flow property profile defined in $[z_0, z_0 + l]$ is to replace the profile with three compressed images of the original with the middle image flipped. This is how the compressive and rotational motions observed in turbulent flows are represented in ODT (Kerstein 1999*a*). The triplet map is adopted because it is the simplest map satisfying the following physical requirements: all moments of the flow properties are preserved by the map, i.e. $\int_0^h s^n(z)\,\mathrm{d}z$ is preserved, where $s = u, v, w, \rho, T, S$, property profiles remain continuous, and changes in the property gradients of order greater than 1 are prevented (Kerstein 1999*a*). The dependence of model results on the use of either the triplet map or another map satisfying the physical requirements has been addressed in a different context (Kerstein 1991). Qualitative behaviours are unaffected and quantitative differences are absorbed in the adjustment of model parameters.

The form of the function $K(z)$ and the constants $c_i = (c_u, c_v, c_w)$ in (2.2) are now discussed (cf. Kerstein *et al.* 2001; McDermott 2005 and Wunsch & Kerstein 2005 for additional details). The operations (2.2) induce a change of kinetic energy associated with a velocity component i of

$$\Delta KE_i = \frac{\rho_0}{2} \int_0^h \left[(u_i(f(z)) + c_i K(z))^2 - u_i^2(z) \right] \mathrm{d}z, \tag{2.4}$$

and a change in potential energy of

$$\Delta PE = g \int_0^h (\rho(f(z)) - \rho(z)) z \,\mathrm{d}z. \tag{2.5}$$

Energy conservation requires $\sum_i \Delta KE_i = -\Delta PE$. Notice in (2.4) that $\Delta KE_i = 0$ if $c_i K(z) = 0$. Hence, the terms $c_i K(z)$ are needed to conserve energy in stratified flows. Furthermore, the terms $c_i K(z)$ allow the introduction of a pressure scrambling mechanism that redistributes the kinetic energy among different velocity components while conserving energy. In other words, the addition of $c_i K(z)$ in (2.2) allows changes in ΔKE_i while enforcing $\sum_i \Delta KE_i = -\Delta PE$. The function $K(z)$ is conveniently defined by

$$K(z) = z - f(z), \tag{2.6}$$

which is the simplest continuous function that modifies property profiles only in the eddy region ($K(z) = 0$ outside $[z_0, z_0 + l]$) while conserving momentum ($\int_0^h K(z)\,\mathrm{d}z = 0$). The function $K(z)$ represents the vertical displacement of fluid elements $z - f(z)$ induced by a triplet map. By using definitions (2.3) and (2.6), expressions (2.4) and

(2.5) become, after some algebraic manipulation,

$$\Delta KE_i = \frac{2}{27}\rho_0 l^3 c_i^2 + \rho_0 l^2 u_{i,K} c_i, \tag{2.7}$$

and

$$\Delta PE = g l^2 \rho_K, \tag{2.8}$$

where

$$s_K = \frac{1}{l^2}\int_0^h s(f(z))K(z)\,\mathrm{d}z, \tag{2.9}$$

with $s = u, v, w, \rho, T, S$ and $\rho_K/\rho_0 = \beta_S S_K - \beta_T T_K$. The pressure scrambling mechanism is modelled by assuming $\Delta KE_i = \alpha(-Q_i + Q_j/2 + Q_k/2)$, where j and k denote indices other than i, α is a constant and Q_i is a function of $u_{i,K}$ only. The function Q_i is assumed to be equal to the maximum amount of energy that can be extracted from a given velocity component, which is obtained by differentiating ΔKE_i with respect to c_i in (2.7), and equals $(27/8)\rho_0 l u_{i,K}^2$. In addition, equipartition of energy among the velocity components gives $\alpha = 2/3$. Finally, a quadratic equation for each of the constants c_i is obtained by using the previous considerations, together with (2.7) and (2.8), and $\sum_i \Delta KE_i = -\Delta PE$, where the terms on the left hand side are incremented equally to satisfy this. The solution of these quadratic equations gives

$$c_i = \frac{27}{4l}\left(-u_{i,K} + \mathrm{sgn}(u_{i,K})\left(\frac{1}{3}\left(\sum_i u_{i,K}^2 - \frac{8}{27} g l \frac{\rho_K}{\rho_0}\right)\right)^{1/2}\right), \tag{2.10}$$

where the summation is over the three velocity components, and sgn is the sign function.

2.3. *Sampling of eddy events*

Each event is characterized by a length scale l and a location z_0 which are randomly sampled from a joint probability density function $p(l, z_0; t)$ defined by

$$p(l, z_0; t) = \frac{\lambda(l, z_0; t)}{\int_0^h \int_0^h \lambda\,\mathrm{d}l\,\mathrm{d}z_0}. \tag{2.11}$$

$p(l, z_0; t)\,\mathrm{d}l\,\mathrm{d}z_0$ can be interpreted as the probability of occurrence of an eddy event of size within the range $[l, l + \mathrm{d}l]$ with its lower boundary located within the range $[z_0, z_0 + \mathrm{d}z_0]$. $\int_0^h \int_0^h \lambda\,\mathrm{d}l\,\mathrm{d}z_0$ is the overall event rate.

The eddy rate distribution λ is given by

$$\lambda = \frac{C}{l^3}\left(\sum_i u_{i,K}^2 - \frac{8}{27} g l \frac{\rho_K}{\rho_0} - Z\left(\frac{\nu}{l}\right)^2\right)^{1/2}, \tag{2.12}$$

if the expression inside the square root is positive, and $\lambda = 0$ otherwise. In (2.12), the summation is over the three velocity components, and C and Z are model parameters, discussed further in § 2.5. Eddy events are sampled independently, but the time dependence of λ correlates these events in time. This feature of ODT generates an energy cascade, as explained in Kerstein (1999*a*).

The eddy rate distribution (2.12) is obtained as follows (cf. McDermott 2005 and Kerstein 2009 for more details). Recognizing that λ has units of length$^{-2} \times$ time^{-1}, and using the eddy length scale l, an eddy mass $\rho_0 l$ and an eddy energy E,

dimensional reasoning gives $\lambda \sim (E/(\rho_0 l))^{1/2}/l^3$. This scaling relationship establishes the dependence between the eddy sampling process, related to λ and l, and the properties of the flow, embodied in E. The eddy energy E is assumed to be the maximum energy extractable using (2.7) upon completion of the eddy event, which equals $\sum_i Q_i$ from the previous discussion, minus the eddy-induced potential-energy change given by (2.8). Hence, the following expression for λ is obtained:

$$\lambda \sim \frac{1}{l^3}\left(\sum_i u_{i,K}^2 - \frac{8}{27} g l \frac{\rho_K}{\rho_0}\right)^{1/2}. \tag{2.13}$$

The eddy rate expression (2.12) is finally obtained by using a proportionality constant C and by inserting the term $-Z(\nu/l)^2$ inside the square root in (2.13), to prevent the occurrence of eddies with a time scale longer than the viscous time scale l^2/ν.

Physically, the eddy rate expression incorporates into ODT the effects of stratification, shear and viscous damping on the turbulent fluctuations, with C determining the generation rate. In (2.12), turbulent fluctuations are generated by shear through $\sum_i u_{i,K}^2$, damped by viscous action through $-Z(\nu/l)^2$ and suppressed (generated) by the salinity (temperature) field through $-(8/27)gl(\rho_K/\rho_0)$, recalling that $\rho_K/\rho_0 = \beta_S S_K - \beta_T T_K$.

2.4. *An assessment of ODT*

ODT has reproduced a variety of turbulence phenomena with a concise representation of the interaction between molecular transport, advection and buoyant forcing. It has captured, for example, the Kolmogorov cascade for velocity fluctuations in homogeneous isotropic turbulence (Kerstein 1999*a*). Nonetheless, ODT is a model that seeks to emulate Navier–Stokes turbulence on a 1D domain. Thus, its results need to be interpreted with care, and compared with other models and available measurements. This approach is taken throughout the present work. Next, three limitations of ODT are discussed.

First, ODT does not capture 3D coherent flow structures and their corresponding effects on the flow. For example, in the simulation of mixing layers and wakes, even though ODT profiles agree reasonably well with those from DNS, the probability density function of the (passive) scalar near the edges differs considerably between ODT and DNS (Kerstein *et al.* 2001). This disagreement is caused by the inability of ODT to capture 3D flow structures occurring in this region (Kerstein *et al.* 2001). For the present problem, ODT does not capture interfacial waves. The effect of these waves on the fluxes across (unsheared) double-diffusive interfaces is still unclear (Turner 1965; Linden & Shirtcliffe 1978; Fernando 1989). Second, ODT is limited to horizontally homogeneous flows, so it cannot be used to study the effect of geometry. As an example, the so-called wind of turbulence of Rayleigh–Bénard convection cannot be studied with ODT, since the geometry of the cell has an important effect on it (Wunsch & Kerstein 2001). Notwithstanding the above two shortcomings, a comparison of ODT results with those from experiments or DNS can be used to determine how sensitive is a particular observable of the flow to the effect of flow structures and geometry. For example, the amplitude of the temperature fluctuations in the core of a Rayleigh–Bénard cell may depend on the cell geometry (Wunsch & Kerstein 2001). However, the shape of the probability density function of these fluctuations is seen to be the same in experiments and ODT, consistent with experimental indications of insensitivity to cell geometry (Wunsch & Kerstein 2001). Finally, a third shortcoming of ODT is that the model constants C and Z need

adjustment for ODT results to agree with those from experiments or DNS. As an example, in wall-bounded flows, Z needs adjustment for ODT to properly capture the transition from the viscous sublayer to the log layer (Schmidt *et al.* 2003). This adjustment is needed because viscous effects are very important near the wall, and Z is the parameter that controls the suppression of the smallest eddies in the flow by viscous action, cf. § 2.5. It is remarkable, nonetheless, that with only two model constants, ODT can capture a wide variety of flow behaviour. In the following, we will see that the effect of C and Z on scaling exponents is not large.

2.5. *Numerical implementation*

The ODT model consists of the following components: the flow boundary and initial conditions; the diffusion equations (2.1); the eddy operations (2.2); the sampling of eddy occurrence times and, using (2.11), eddy sizes and locations; the discrete implementation of the diffusion equations and the eddy operations; and the two free parameters C and Z.

Two flow configurations are considered. In the jump-periodic configuration, the following boundary conditions are applied to the diffusion equations (2.1):

$$u(t, z=h) = u(t, z=0) + \Delta U, \quad v(t, z=h) = v(t, z=0), \quad w(t, z=h) = w(t, z=0), \tag{2.14}$$

$$T(t, z=h) = T(t, z=0) + \Delta T, \quad S(t, z=h) = S(t, z=0) + \Delta S. \tag{2.15}$$

For the rundown configuration, the following boundary conditions are used:

$$\frac{\partial s}{\partial z}|_{t,z=0} = \frac{\partial s}{\partial z}|_{t,z=h} = 0, \tag{2.16}$$

where $s = u, v, w, T, S$. In addition, in the jump-periodic (rundown) configuration, triplet maps are allowed (prevented) across $z=0$ and $z=h$. For the initial conditions given below, the flow is seen to reach a quasi-steady state with jump-periodic boundary conditions, while it remains unsteady in the rundown configuration. In contrast with previous studies, which use either a heated-bottom or a rundown configuration (cf. § 1), most of the results presented here are for the jump-periodic configuration. Because they are obtained from quasi-steady conditions, these results are not contaminated by time-dependent effects and can be compared with available steady-state theories. Selected results for the rundown configuration are presented in § 3.4, though.

The initial conditions are

$$u(t=0, z) = \Delta U \left[\frac{1}{2} + \frac{1}{2}\tanh\left(\frac{z - h/2}{\delta_u/2}\right)\right] + r, \tag{2.17}$$

$$v(t=0, z) = 0, \quad w(t=0, z) = 0, \tag{2.18}$$

$$T(t=0, z) = \Delta T \left[\frac{1}{2} - \frac{1}{2}\tanh\left(\frac{z - h/2}{\delta_T/2}\right)\right], \tag{2.19}$$

$$S(t=0, z) = \Delta S \left[\frac{1}{2} - \frac{1}{2}\tanh\left(\frac{z - h/2}{\delta_S/2}\right)\right], \tag{2.20}$$

where $\delta_u = \delta_T = 0.1h$, $\delta_S = 0.01h$ and r is a small random perturbation. We observe only a slight dependence of the observables studied here on the choice of δ_u, δ_T, δ_S and r, the shear direction, and the use of profiles similar to the ones above but with functions other than tanh. With these initial conditions, a single double-diffusive interface is considered, as done in previous studies (e.g. Turner 1965; Crapper 1975;

Marmorino & Caldwell 1976; Linden & Shirtcliffe 1978; Fernando 1989; Worster 2004). While the study of a single interface is more fundamental, that of multiple interfaces is of more practical relevance and should be considered in the future (cf. § 5).

Direct sampling of eddy events requires the reconstruction of the probability density function $p(l, z_0; t)$ as the flow evolves. This costly operation is avoided by using a Monte Carlo method called thinning (Kerstein 1999*a*; Law & Kelton 2000). The application of this method in ODT is described elsewhere (cf. Kerstein 1999*a*; McDermott 2005).

The diffusion equations and the triplet map are implemented using a first-order finite-volume scheme with a non-uniform adaptive mesh (cf. Krishnamoorthy 2008; Ricks *et al.* 2010 for more details). This approach allows accurate resolution of regions of the flow with very large property gradients. Within this framework, the flow property profiles within a given finite volume are uniform, and the finite volumes can be split, displaced and merged. Additionally, the application of the triplet map involves three steps. First, the finite volumes containing z_0 and $z_0 + l$ are split at these respective locations. Second, each finite volume in the eddy region $[z_0, z_0 + l]$ is split into three identical volumes, each of width one-third of the width of the original volume. Third, the new finite volumes are displaced to mimic the alteration of the property profiles given by the continuous triplet map (2.3). Triplet maps are implemented only for eddies spanning at least six finite volumes. This finite-volume triplet map retains the characteristics of its continuous counterpart.

The splitting and displacement of finite volumes or cells by the triplet map may produce a mesh structure that can degrade computational accuracy and efficiency. Hence, the last component of the discrete implementation is a mesh management strategy. With this strategy, the splitting and merging of finite volumes is performed considering the following factors: cell size, gradient resolution, curvature resolution and cell size variation. Grid cells that are below a specified minimum size are merged with neighbouring cells until the cell is enlarged above the minimum size. Offending cells are treated in order of increasing size, and merging is done with the smaller of the two neighbouring cells. This is done in a manner that precludes any directional bias in the merging. Cells are merged if the variation in a specified property field (e.g. velocity) is below a specified fraction of the total variation in that field. The same is done for changes in the slope of the profile. Cells are split if the variation in the property field, or its slope, is greater than a specified fraction of the total variation in that field. Finally, cells are split in order to maintain the ratio of adjacent cell sizes (size of the larger of a pair of cells divided by the size of the smaller cell of the pair) between 1 and 2.5. This procedure results in an efficient computational grid, with good resolution of property fields with high gradients or regions of high curvature, while avoiding abrupt variations in the grid. Five mesh adaption parameters are specified with the current approach (small cell and upper and lower thresholds for gradients and curvature). The parameters used here are selected so that the ODT solutions are approximately independent of them, i.e. the results presented here are approximately grid independent. A similar mesh management strategy was used and verified by Krishnamoorthy (2008).

The model parameter C determines the strength of the turbulence in ODT. Low values of C, say $C < 0.1$, give a low rate of occurrence of eddies, from (2.11) and (2.12), and consequently almost no eddies are implemented. In other words, when C is small enough, the flow is laminar. Such a condition is of no interest here. On the other hand, large values of C produce a lot of eddies, and thus the flow is very turbulent. We observe that for $C > 1000$ so many eddies are implemented that the

simulations become computationally very expensive for the ranges of Ra and Ri considered. Therefore, we vary C over $C = 1$–100 to test the results presented here for their sensitivity to C. The viscous cutoff parameter Z controls the suppression of the smallest eddies of the flow by viscous action. Notice in (2.12) that for fixed Z and small-enough eddy size l, the term inside the square root can become negative, in which case the eddy is not implemented. As with small values of C, large values of Z, say $Z > 1000$, produce a laminar flow, which is of no interest here. We observe that the variation of Z when $Z < 0.001$ has almost no effect on the flow. Thus, we consider the range $Z = 0.01$–100 to test the results presented here for their sensitivity to Z.

The ODT model is made dimensionless for numerical simulation by using h, h^2/ν and ρ_0 as length, time and density scales, respectively, and by making the temperature and salinity dimensionless with β_T and β_S.

2.6. *ODT observables*

ODT simulations generate flow realizations, i.e. time sequences of the instantaneous snapshots of the flow field. For a quasi-steady flow, only one realization is needed to obtain a time average of an observable. On the other hand, when the flow is transient, an ensemble of realizations is used, from which an observable is averaged for each time t.

In ODT, for quasi-steady flows, the turbulent kinetic energy per unit mass TKE is calculated as

$$TKE = \frac{1}{2}\sum_i (u_i')^2, \tag{2.21}$$

and the viscous dissipation ε is given by

$$\varepsilon = \nu \sum_i \left(\frac{\partial u_i'}{\partial z}\right)^2, \tag{2.22}$$

where $u_i' = u_i - \langle u_i \rangle_t$, and $\langle\ \rangle_t$ denotes a time average. The time and spatial average of TKE is used to define a Reynolds number as follows:

$$Re = \frac{(\langle\langle TKE\rangle_z\rangle_t)^{1/2} h}{\nu}, \tag{2.23}$$

where $\langle\ \rangle_z$ denotes a spatial average. This average is taken away from the interface where the velocity fluctuations are damped. Notice that Re is not an independent variable but an observable representing a measure of the velocity fluctuations induced by thermal convection. Similarly, a time and spatial average of ε is used and is denoted by $\langle\langle\varepsilon\rangle_z\rangle_t$.

The vertical flux F_s of the flow property s is expressed as $F_s = F_s^{diff} + F_s^{adv}$, where $s = u, T, S$, and F_s^{diff} and F_s^{adv} are respectively the diffusive and advective fluxes of s. Here F_s, F_s^{diff} and F_s^{adv} represent fluxes that are temporally averaged over a time interval Δt and spatially averaged along the computational domain. F_s^{diff} is found by temporally and spatially averaging the diffusive fluxes $-\kappa_s(\partial s/\partial z)$ across the finite-volume faces, where $\kappa_s = \nu, \kappa_S, \kappa_T$. The advective flux F_s^{adv} is produced by the vertical displacement of fluid elements induced by triplet maps and can be interpreted as the ODT analogue of $\langle\langle w's'\rangle_z\rangle_t$ calculated in a Navier–Stokes simulation. This flux is calculated as

$$F_s^{adv} = \frac{1}{h\Delta t}\sum_{eddies}\int_0^h s(f(z))K(z)\,\mathrm{d}z, \tag{2.24}$$

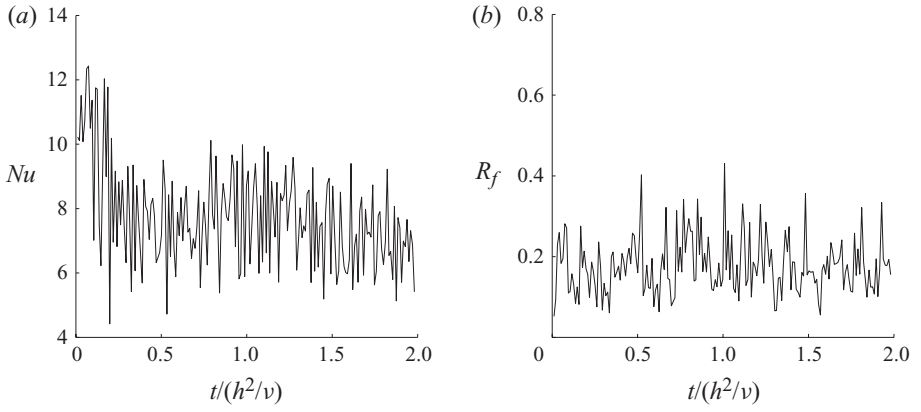

FIGURE 1. Temporal evolution in the jump-periodic configuration of (a) the dimensionless heat flux Nu and (b) the buoyancy ratio R_f. Parameter values are $R_\rho = 7$, $Ra = 10^8$, $Le = 0.01$, $Pr = 7$, $C = 10$ and $Z = 1$.

where $\sum_{eddies}$ denotes a summation over all the eddies implemented during the time interval Δt. Recalling that $K(z)$ represents the vertical displacement of fluid elements induced by a triplet map, this expression follows from the assumed spatial homogeneity and the definition of the flux of s as $1/\Delta t$ times the net transfer of property s across any location z during Δt.

With jump-periodic boundary conditions the fluxes F_T and F_S are observed to be approximately spatially uniform (not shown). In the rundown configuration, for a given time, these fluxes decrease approximately linearly from a maximum value at $z/h \approx 0.5$ to a value of zero at $z/h = 0$ and $z/h = 1$ (not shown). Thus, the spatial averaging has no effect on how F_T and F_S scale with the governing parameters in either configuration.

Figure 1 shows a typical time variation of the fluxes for the jump-periodic configuration. Notice in figure 1(a) that, after an initial transient, the heat flux reaches a quasi-steady state, where it fluctuates around a mean value. Other observables were seen to behave similarly (not shown). Throughout the present work the fluxes and other observables are time averaged during this quasi-steady state for the jump-periodic configuration. On the other hand, because the flux is unsteady in the rundown configuration, the fluxes are ensemble averaged. This is further discussed in § 3.4.

2.7. *Verification*

For the present application, the variable-mesh code developed was tested for accuracy and consistency by verifying its results with those from the uniform-mesh code BasicODT (Kerstein 2007). Figure 2 shows the ratio of buoyancy fluxes R_f predicted by the code used in the present work and by BasicODT. The largest discrepancy is 11 %. This is acceptable for the study conducted here.

3. Unsheared interfaces

The representation of double-diffusive convection in the diffusive regime by ODT is explained next in § 3.1 (cf. also Kerstein 1999*b*). This is followed by discussions of the effect of R_ρ, Ra, Pr and Le on the fluxes of heat and salt across unsheared interfaces in §§ 3.2–3.6. Additionally, the effect of these parameters on the intensity of the convection, represented by Re, is considered.

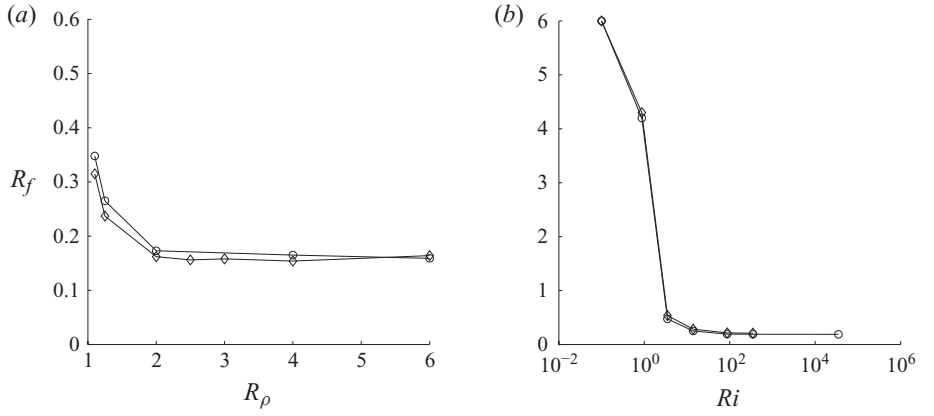

FIGURE 2. Comparison of the predicted ratio of buoyancy fluxes R_f between the variable-mesh code used in the present work (diamonds) and the uniform-mesh code BasicODT by Kerstein (2007) (circles). (*a*) Effect of R_ρ in unsheared interfaces for $Ra = 10^8$, $Le = 0.01$ and $Pr = 7$. (*b*) Effect of Ri for $R_\rho = 6$, $Ra = 5 \times 10^8$, $Le = 0.0125$ and $Pr = 7$. Model parameter values are $C = 10$ and $Z = 100$. The largest discrepancy is 11 %.

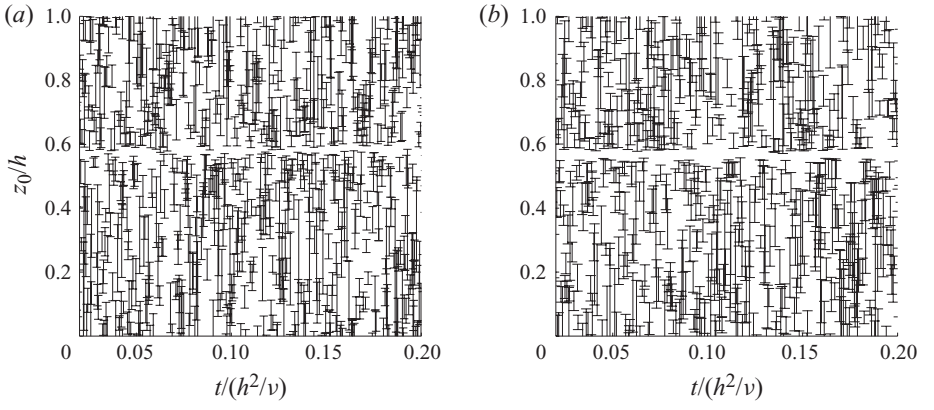

FIGURE 3. Temporal sequence of the locations z_0 and sizes l (vertical bars) of eddy events generated in an ODT simulation of double-diffusive convection. Every eddy event implemented in the simulations is shown for the time interval $0.2\,(h^2/\nu)$. Parameter values are $Ra = 10^8$, $Le = 0.01$, $Pr = 7$, $C = 10$, $Z = 1$, and (*a*) $R_\rho = 2$ and (*b*) $R_\rho = 4$. Notice the more aggressive erosion of the interface at the lower value of R_ρ.

3.1. *Flow description*

Figure 3 shows the temporal sequence of the locations z_0 and sizes l, denoted with vertical bars, of eddy events generated during two ODT simulations at different values of R_ρ. These eddy events are sampled in the manner described in § 2.3. They modify the flow property profiles through the operations (2.2). Figure 4 shows time-averaged density profiles. The characteristic structure of double-diffusive convection in the diffusive regime is evident in figures 3 and 4: a double-diffusive interface can be seen in figure 3 as a region near $z/h \approx 0.57$ where eddies are suppressed, while it appears in figure 4 as a sharp density gradient around $z/h \approx 0.57$. This interface separates well-mixed convective regions where the turbulent activity is strong, cf. figure 3, and the time-averaged flow properties are approximately constant with z, cf.

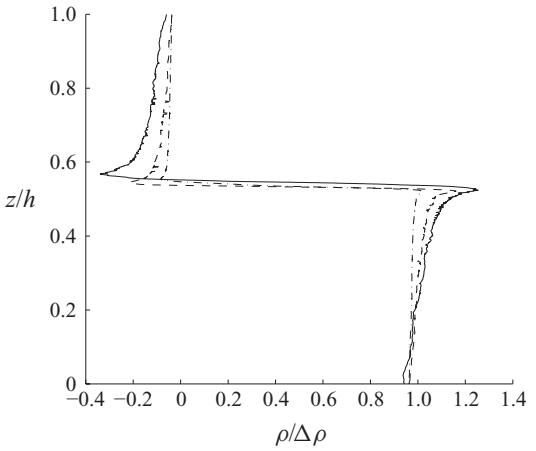

FIGURE 4. Effect of R_ρ on the time-averaged density $\rho/\Delta\rho$ profiles, where $\Delta\rho = \beta_S \Delta S - \beta_T \Delta T$. Parameter values are $R_\rho = 1.5$ (solid line), 2 (dashed line), 4 (dash-dotted line), and $Ra = 10^8$, $Le = 0.01$, $Pr = 7$, $C = 10$ and $Z = 1$. The unstable stratification near the edges of the diffusive interface generates convective motions that 'lift' the salt.

figure 4 for density. The unstable density stratification near the interface, noticeable in figure 4, generates convective motions. The distinctive coupling between molecular transport and turbulent convection is represented in ODT as follows. The much higher diffusivity of heat than salt generates the unstable stratification producing turbulent convective motions. These motions, in turn, transport the heat and salt from the edges of the interface into the mixed regions, and may penetrate the interface, cf. figure 3(*a*). This eroding process has been observed in experiments (Fernando 1989) and also in previous ODT simulations (Kerstein 1999*b*). The convective motions, thus, sharpen the temperature and salinity profiles at the interface, modifying the molecular transport of heat and salt there. For quasi-steady-state conditions, the transport by the convective motions is balanced by the molecular transport, as long as the interface is not heavily eroded or broken; otherwise, the transport of heat and salt is determined by turbulent motions. The dominant transport mechanism depends on R_ρ, as discussed next, and on Ri, as discussed later in § 4.

3.2. *Effect of* R_ρ

The stability parameter R_ρ represents the ratio of the stabilizing effect of salinity and the destabilizing effect of temperature. We consider here the range $R_\rho = 1.05$–8, $Pr = 7$ and $Le = 0.01$. The regime $R_\rho \gtrsim 10$ is not explored here but has previously been studied with ODT (Kerstein 1999*b*). ODT simulations show that when $R_\rho \lesssim 2$ eddies heavily erode the interface and may penetrate into it, cf. figure 3(*a*). The interface is said to be unstable. Thus, the transport of heat and salt is due to turbulent entrainment and R_f increases with decreasing R_ρ (Turner 1979), as can be seen in figure 5(*a*). On the other hand, these simulations show that when $R_\rho \approx 2$–8, the ratio R_f reaches an approximately constant value, cf. figure 5(*a*). This can be interpreted as a balance between convective and molecular transport (Linden & Shirtcliffe 1978; Turner 1979, p. 277). The interface is said to be stable, and the regime is referred to as the constant-R_f regime.

A comparison between figures 5(*a*) and 5(*b*) shows that the trends predicted by ODT simulations agree with results from bottom-heating experiments. Notice in these figures that results from simulations with $C = 10$ and $Z = 100$ are consistent

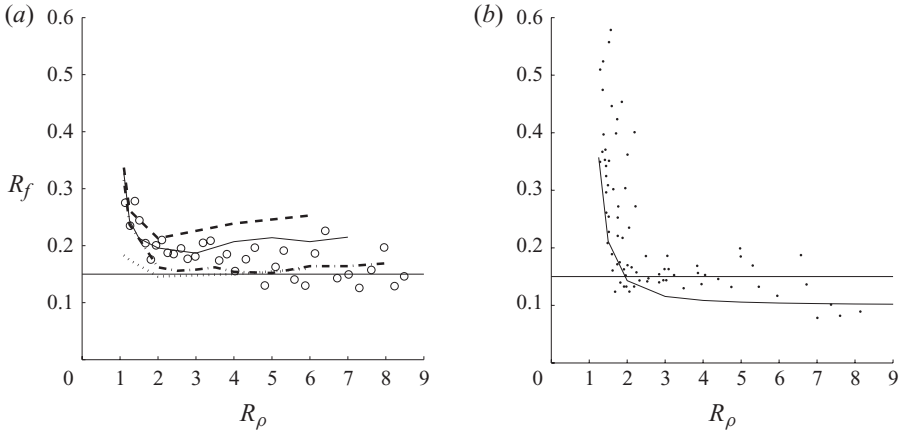

FIGURE 5. Effect of R_ρ on the ratio of buoyancy fluxes R_f. (*a*) Simulation results for the jump-periodic (lines) and rundown (circles) configurations. (*b*) Results from bottom-heated experiments compiled by Kelley (1990) (dots) and the theoretical prediction by Linden (1974) (solid line). Parameter values of the simulations are $Ra = 10^8$, $Le = 0.01$ and $Pr = 7$. Model parameter values are $C = 10$ and $Z = 1$ (solid line), $C = 10$ and $Z = 100$ (dash-dotted line), $C = 1$ and $Z = 1$ (dotted line), $C = 10$ and $Z = 0.01$ (dashed line), and $C = 10$ and $Z = 1$ for the rundown configuration. The fluxes are ensemble averaged over 10 realizations with the rundown configuration. The horizontal lines denote $R_f = 0.15$. Both experiments and ODT simulations show that turbulent entrainment dominates when $R_\rho \lesssim 2$, and that molecular processes become important when $R_\rho \gtrsim 2$, giving an approximately constant value of R_f. ODT results for $C = 10$ and $Z = 100$ agree well with experimental data.

with those measured in the experiments. It is difficult, however, to quantify the agreement between results from these ODT simulations and those from experiments when $R_\rho \lesssim 2$ because of the large scatter of experimental data (Kelley 1990).

The foregoing physical picture is incorporated in the model by Linden (1974) as follows. This model is discussed here since it incorporates the effects of R_ρ and Le on R_f in a simple theoretical framework. The fluxes of heat and salt are divided into double-diffusive and entrainment components. The former arises from convective motions generated by the double-diffusive instability that do not penetrate the interface, while the latter is due to motions that heavily erode the interface and can penetrate into it. These components are assumed to be additive. The ratio of the double-diffusive components of the salt and heat fluxes is assumed to be equal to $Le^{1/2}$ by an argument discussed later. A $Ri^{-3/2}$-entrainment law is used to model the entrainment components of the fluxes (Fernando 1991). The above arguments lead to

$$R_f = \frac{C_{l74} R_\rho + Le^{1/2}(R_\rho - 1)^{3/2}}{C_{l74} + (R_\rho - 1)^{3/2}}, \tag{3.1}$$

where C_{l74} is an adjustable constant, set to 0.05 in Linden (1974). Figure 5 shows that (3.1) is within the results from experiments and from ODT simulations with $C = 10$ and $Z = 100$.

By increasing R_ρ the overall stratification becomes stronger and the regions of unstable stratification at the edges of the diffusive interface become less pronounced, cf. figure 4. Consequently, the convection is slowed down and the heat flux is reduced. Figure 6 shows that this trend is seen in both ODT simulations and bottom-heated experiments. Also notice in figure 6 that results from ODT simulations with $C = 10$ and $Z = 100$ in the range $R_\rho \approx 2$–8 are within 20 % of those obtained in bottom-heated

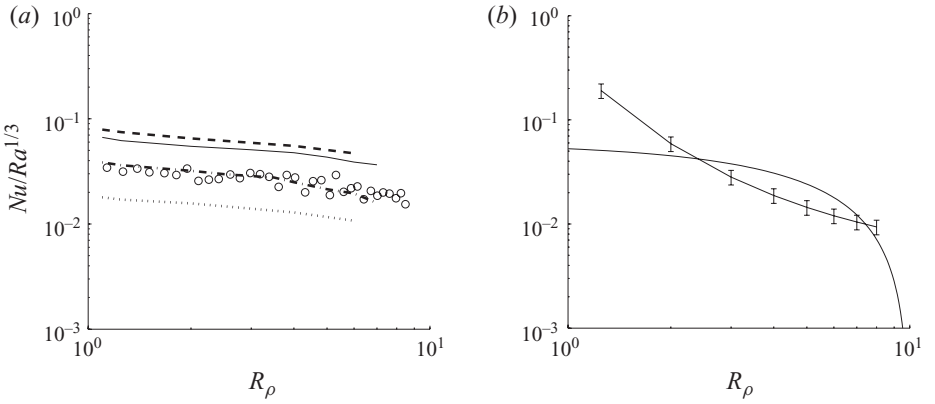

FIGURE 6. Effect of R_ρ on the dimensionless heat flux Nu. (*a*) Simulation results for the jump-periodic (lines) and rundown (circles) configurations. (*b*) Empirical fit by Kelley (1990) using data from bottom-heated experiments (solid line with error bars) and the theoretical prediction by Linden & Shirtcliffe (1978) (solid line). The error bars denote the average deviation of 32 % from the experimental data reported by Kelley (1990). Parameter values of the simulations are the same as in figure 5. The stratification becomes stronger as R_ρ increases, and the heat flux Nu decreases accordingly.

experiments. A comparison between results from ODT simulations and those from experiments when $R_\rho \lesssim 2$ is not made here since, in addition to the large scatter of the experimental data discussed previously, there are mechanisms in the bottom-heated experiments when $R_\rho \lesssim 2$ that are not present with the configurations used in the present work. These mechanisms include the distortion of the double-diffusive interface by the impingement on the interface of convective elements generated at the heated bottom, and by the grid stirring used in some of the experiments (Worster 2004). Further comparisons between ODT results and those from bottom-heated and rundown experiments are given in Kerstein (1999*b*).

Figure 6 also shows that when $R_\rho \lesssim 6$, results from ODT simulations with $C = 10$ and $Z = 100$ and $Z = 1$ agree well with predictions from the model by Linden & Shirtcliffe (1978). This model predicts Nu as a function of Ra, R_ρ and Le by considering a diffusive interface with regions of unstable stratification at its edges, and by assuming steady-state conditions, so that molecular fluxes across the interface are balanced by convective fluxes. As discussed above, this flow structure and flux balance are observed with ODT simulations in the range $R_\rho \approx 2$–8. The convective flux is assumed by Linden & Shirtcliffe (1978) to occur as a cyclic eruption of boundary layers: at the edges of the diffusive interface unsteady boundary layers grow with time, and once a critical Rayleigh number (based on the boundary layer thickness) is reached, the boundary layers detach, transporting with them heat and salt into the well-mixed regions. Within this picture, as Le increases (recall that $Le = \kappa_S/\kappa_T$) more salt diffuses into the unstable regions before they erupt, so that R_f increases with Le as $R_f = Le^{1/2}$ (cf. § 3.6 and Turner 1979, p. 277). By further assuming $Nu/Ra^{1/3} = F(R_\rho, Le)$ the following expression for Nu is obtained:

$$\frac{Nu}{Ra^{1/3}} = C_{l78}\frac{(1 - Le^{1/2}R_\rho)^{4/3}}{(1 - Le^{1/2})^{1/3}}, \tag{3.2}$$

where $C_{l78} = 0.0587$. This model has been modified to include time-dependent effects (Worster 2004).

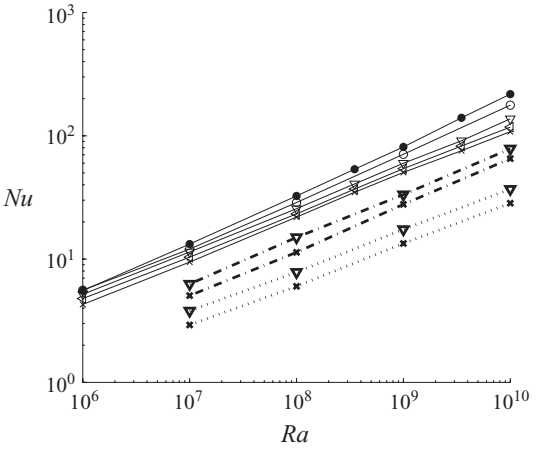

FIGURE 7. Effect of Ra on Nu. Parameter values are $R_\rho = 1.05$ (dots), 1.25 (circles), 2 (inverse triangles), 3 (left triangles), 4 (crosses), $Le = 0.01$, and $Pr = 7$. Model parameter values are $C = 10$ and $Z = 1$ (solid lines), $C = 10$ and $Z = 100$ (dashed-dotted lines), and $C = 1$ and $Z = 1$ (dotted lines). ODT results give $Nu \sim (Ra/R_\rho)^{0.37\pm0.03}$. Here (Ra/R_ρ) can be seen as the ratio of destabilizing and stabilizing effects.

The ODT parameter C controls the generation rate of turbulent fluctuations, cf. § 2.3. Hence, higher values of C are associated with higher levels of interface erosion and, thus, higher R_f and Nu. This can be seen in figures 5 and 6, where an increase of C from 1 to 10 at fixed Z produces increases of R_f and Nu. Similarly, lower values of Z produce a more aggressive erosion of the interface (not shown) and, consequently, lead to an increase of R_f and Nu, as can be seen in figures 5 and 6, where Z is varied from 0.01 to 100. Even though C and Z have a noticeable effect on R_f and Nu, their effect on how these observables scale with the dominant parameters is rather small, as shown next.

3.3. *Effect of Ra*

The scaling of flow observables with Ra predicted by ODT simulations has been observed to agree well with experiments and DNS in the problems of Rayleigh–Bénard convection (Wunsch & Kerstein 2005) and vertical slot convection (Dreeben & Kerstein 2000). Such a scaling is discussed next for the present problem. The following parameters are considered: $R_\rho = 1.05$–6; $Ra = 10^6$–10^{10}; $Pr = 7$; $Le = 0.01$; $C = 1$, 10 and $Z = 0.01$, 1, 100.

Figures 6 and 7 show, respectively, that Nu depends on R_ρ and Ra through power laws. Hence, data from ODT simulations can be fitted to $Nu \sim (R_\rho)^{n_{R_\rho}}(Ra)^{n_{Ra}}$, where n_{R_ρ} and n_{Ra} are the exponents to be found. This expression is chosen for simplicity, even though observables in thermal convection are seen to be better described with a linear combination of power laws (Grossmann & Lohse 2000). Also notice in figure 7 that the exponent of the power law relating Nu to Ra depends slightly on the model parameters C and Z. Here we fit ODT results to the previous expression for each combination of C and Z in order to calculate the sensitivity of the exponents to these parameters. This sensitivity is expressed by the range of values over which the exponents are seen to vary. The following correlation is obtained with least-squares minimization:

$$Nu \sim (Ra/R_\rho)^{0.37\pm0.03}, \tag{3.3}$$

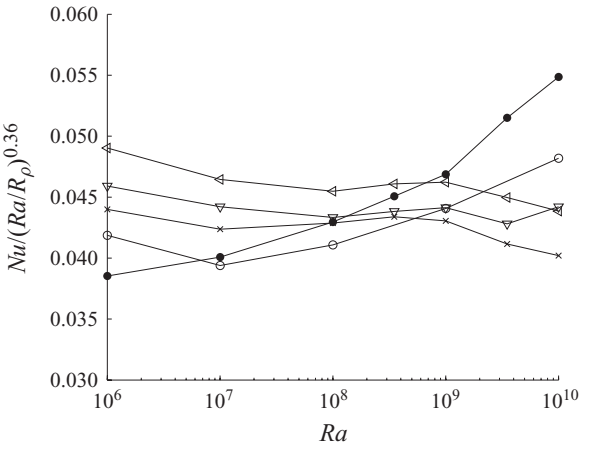

FIGURE 8. *Nu* correlation obtained for $C = 10$ and $Z = 1$. Parameter values are the same as in figure 7.

with an average (maximum) deviation of the data of 6 % (18 %). The range in the exponent denotes its sensitivity to C and Z. This notation is used throughout § 3, unless stated otherwise. The dimensionless group Ra/R_ρ is not assumed *a priori* but is a result of the least-squares minimization. It is interesting that Ra/R_ρ appears as a dominant parameter. This parameter can be interpreted as the ratio of destabilizing and stabilizing effects. Figure 8 shows that the dependence of Nu on Ra and R_ρ is well captured, albeit with some systematic residual dependence on R_ρ, by $Nu \sim (Ra/R_\rho)^{0.36}$ when $C = 10$ and $Z = 1$. Here the value of the exponent is that found for these model parameters.

A comparison is now made with the scaling of Nu with Ra found in Rayleigh–Bénard convection at large Rayleigh numbers. In this form of convection, ODT simulations show that $Nu \sim Ra^{0.3\pm0.03}$ when $Ra = 10^6$–10^{12} (Wunsch & Kerstein 2005), with the range in the exponent denoting its sensitivity to Pr, C and Z. Recent experiments using water ($Pr \approx 4.4$) show $Nu \sim Ra^{0.3\pm0.03}$ when $Ra = 10^8$–10^{11} (Funfschilling *et al.* 2005). Additionally, mixing-length ideas result in $Nu \sim Ra^{1/3}$ when $Pr \gtrsim 0.1$ (Siggia 1994). This expression can also be obtained with dimensional analysis by assuming no interaction between the top and bottom walls, so that the heat flux F_T is independent of h. In comparison, the present results for double-diffusive convection suggest that Nu depends on Ra through a power law with an exponent slightly larger than that observed in Rayleigh–Bénard convection.

The Reynolds number Re defined by (2.23) can be seen as a measure of the velocity fluctuations induced by thermal convection. Notice in figure 9 the power-law increase of Re with Ra. The following correlation for Re is obtained using the same approach as for Nu:

$$Re \sim Ra^{0.45\pm0.04} R_\rho^{-0.12\pm0.05}. \tag{3.4}$$

The average (maximum) deviation of the data is 7 % (15 %). Figure 10 shows how (3.4) fits the data when $C = 10$ and $Z = 1$.

With regard to the effect of Ra on R_f, we observe that R_f increases with Ra when $R_\rho = 1.05$ and 1.25, and that this tendency is reduced for increasing R_ρ. This is shown in figure 11 for $C = 10$ and $Z = 1$ and is seen for other model parameters (not shown).

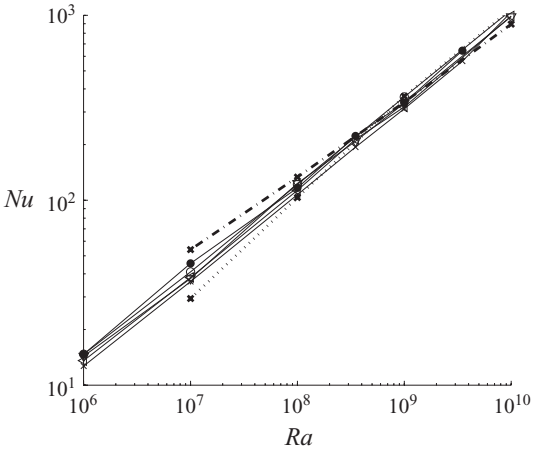

FIGURE 9. Effect of Ra on Re. Parameter values are the same as in figure 7. ODT simulations show that $Re \sim Ra^{0.45\pm0.04} R_\rho^{-0.12\pm0.05}$.

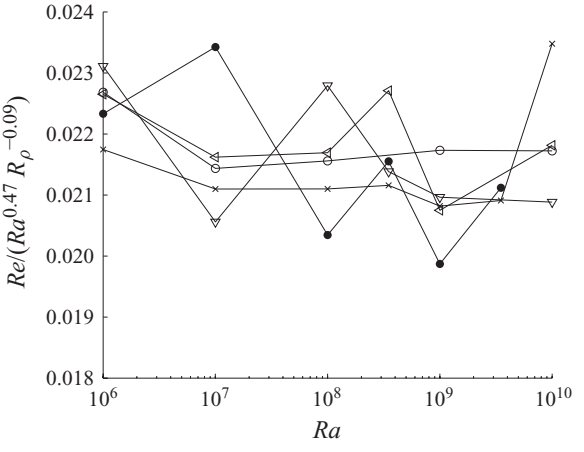

FIGURE 10. Re correlation obtained for $C = 10$ and $Z = 1$. Parameter values are the same as in figure 7.

The larger sensitivity of R_f to Ra at smaller values of R_ρ may explain in part the large scatter of experimental data observed at these values.

3.4. *Effect of boundary conditions*

Next we show that (3.3) is also valid in the rundown configuration. Because in this configuration the flux is zero at the boundaries, the differences of temperature ΔT and salinity ΔS across the interface decrease with time as the two fluid layers mix. As a result, the governing parameters R_ρ and Ra vary with time, cf. figure 12(a), and the fluxes decrease with time, cf. figure 12(b). The initial value of R_ρ is set to 1.1 and that of Ra is set to a value in the range 10^7–10^{10}. Other parameter values are $Le = 0.01$, $Pr = 7$, $C = 10$ and $Z = 1$. Since the flow is unsteady, ensemble averages over 10 realizations are used, i.e. 10 sets of temporal curves like those shown in figure 12 are ensemble averaged. The effect of R_ρ on R_f and Nu is similar in both the jump-periodic and rundown configurations, cf. figures 5 and 6. The combined effect

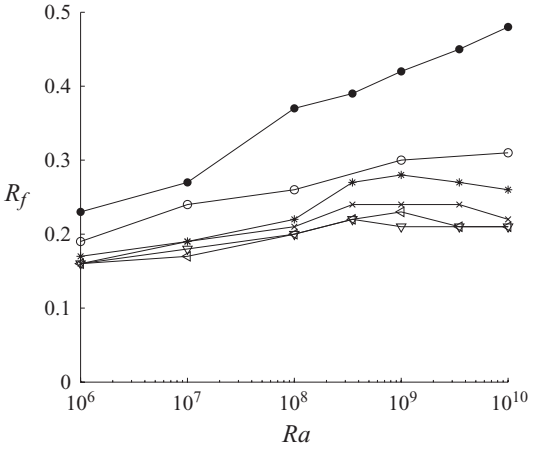

FIGURE 11. Effect of Ra on R_f. Parameter values are the same as in figure 7. The larger sensitivity of R_f to Ra at smaller values of R_ρ may explain the large scatter of experimental data observed at these values.

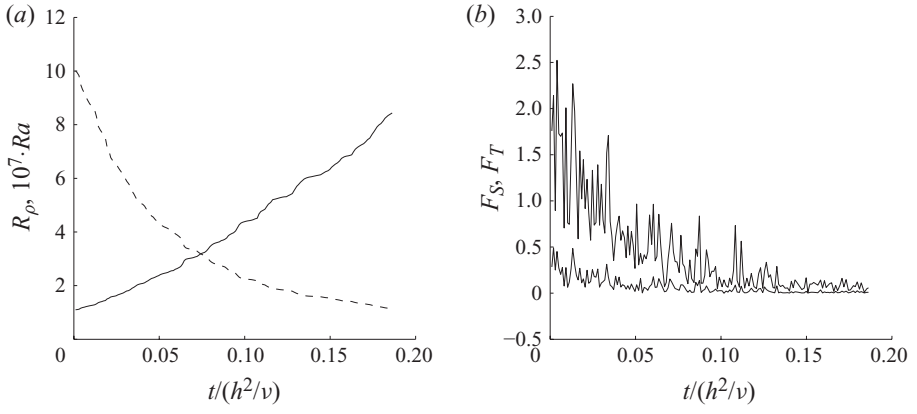

FIGURE 12. Temporal evolution in the rundown configuration of (a) the governing parameters R_ρ (solid line) and Ra (dashed line), and (b) the heat (upper curve) and salt (lower curve) fluxes in arbitrary units. Initial values of $R_\rho = 1.1$ and $Ra = 10^8$ are used. Other parameter values are $Le = 0.01$, $Pr = 7$, $C = 10$ and $Z = 1$. Results from one unsteady simulation are shown.

of R_ρ and Ra on Nu for the rundown configuration is shown in figure 13. With the data in figure 13, the least-squares minimization procedure described previously gives

$$Nu \sim (Ra/R_\rho)^{0.35}, \tag{3.5}$$

with an average (maximum) deviation of the data of 8 % (19 %). The sensitivity of the exponent to the model parameters is not explored. Figure 14 shows how this correlation fits the data. This correlation is close enough to (3.3) to consider the effect of the boundary conditions used here on the scaling of Nu with Ra negligible.

3.5. *Effect of Pr*

The subsequent discussion on the effect of Pr is based on data from simulations with the following parameters: $R_\rho = 2$–6; $Ra = 10^6,\ 10^7,\ 10^8$; $Pr = 0.01$–100; $Le = 0.01$; $C = 1, 10$; and $Z = 1, 100$.

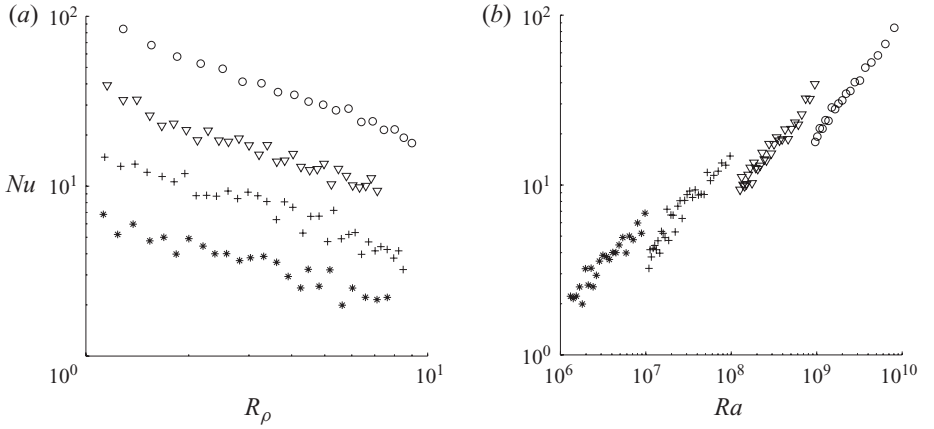

FIGURE 13. Normalized heat flux Nu in the rundown configuration. Initial values used are $R_\rho = 1.1$ and $Ra = 10^7$ (asterisks), 10^8 (plus signs), 10^9 (inverse triangles) and 10^{10} (circles). Other parameter values are $Le = 0.01$, $Pr = 7$, $C = 10$ and $Z = 1$. Results from an ensemble average over 10 unsteady simulations are shown. ODT results for the rundown configuration give $Nu \sim (Ra/R_\rho)^{0.35}$. This result is close to the relationship (3.3) obtained with the jump-periodic configuration.

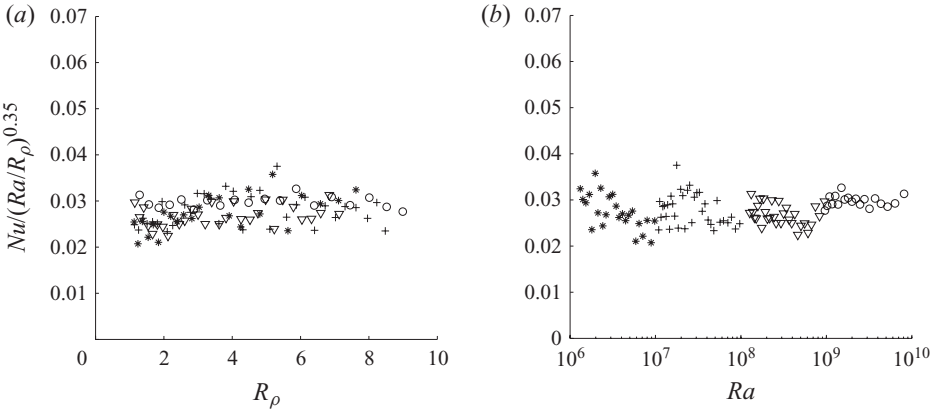

FIGURE 14. Nu correlation obtained for the rundown configuration using least-squares minimization. Parameter values are the same as in figure 13.

Figure 15 shows a power-law increase of Nu with Pr when $Pr = 0.01$–1. Hence, the simulation data are fitted to $Nu \sim (Ra/R_\rho)^n (Pr)^{n_{Pr}}$, where n and n_{Pr} are the exponents to be found. The following correlation is obtained:

$$Nu \sim (Ra/R_\rho)^{0.31} Pr^{0.22\pm0.04}, \quad \text{when } Pr = 0.01\text{–}1, \tag{3.6}$$

with an average (maximum) deviation of the data of 8 % (17 %). The sensitivity of the exponent of (Ra/R_ρ) in (3.6) to C and Z is not explored here. The value of this exponent is for $C = 10$ and $Z = 1$. Figure 16 shows how (3.6) fits the data when $C = 10$ and $Z = 1$ using values of the exponents obtained for these parameters. In comparison, ODT simulations of Rayleigh–Bénard convection for $Ra = 10^9$ show $Nu \sim Pr^{0.23\pm0.03}$ when $Pr \lesssim 1$ (using the data in figure 2 of Wunsch & Kerstein 2005). This scaling relationship agrees with (3.6). Rayleigh–Bénard convection experiments

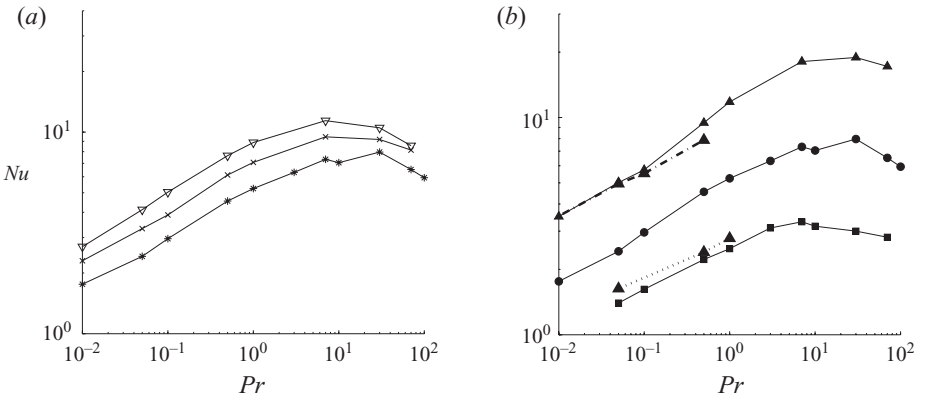

FIGURE 15. Effect of Pr on Nu. (a) $Ra = 10^7$, $R_\rho = 2$ (inverse triangles), 4 (crosses) and 6 (asterisks). (b) $R_\rho = 6$, $Ra = 10^6$ (solid squares), 10^7 (solid circles), 10^8 (solid triangles). Other parameter values are $Le = 0.01$, $C = 10$ and $Z = 1$ (solid lines), $C = 10$ and $Z = 100$ (dash-dotted line), and $C = 1$ and $Z = 1$ (dotted line). Notice that Nu increases (slightly decreases) with Pr when $Pr \lesssim 10$ ($Pr \gtrsim 10$).

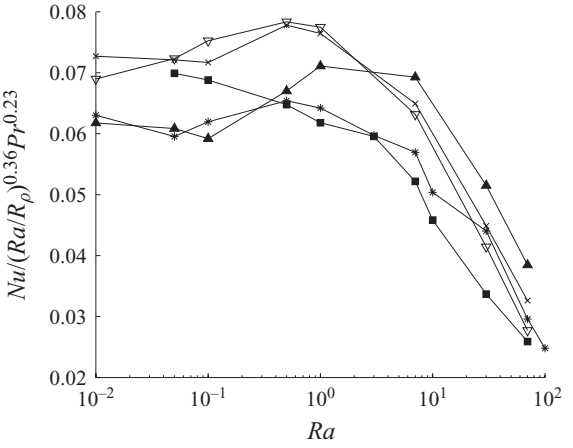

FIGURE 16. Nu correlation obtained for $C = 10$ and $Z = 1$. Parameter values are the same as in figure 15.

for $Ra \sim 10^5$–10^7 indicate the same trend, but a weaker dependence, with $Nu \sim Pr^{1/8}$ for $Pr \lesssim 1$ (Ahlers, Grossmann & Lohse 2009).

Also notice in figure 15 that Nu slightly decreases with Pr for $Pr \approx 10$–100. Not enough data are obtained here to quantify such a decrease. It is found, however, that $Nu \sim (Ra/R_\rho)^{0.36}$ for $Pr = 3$–100. This is consistent with (3.3), which is based on parameter variations for $Pr = 7$. A decrease of Nu with increasing Pr has also been observed in Rayleigh–Bénard convection: ODT simulations show $Nu \sim Pr^{-0.1\pm0.02}$ when $Pr \gtrsim 10$ (using the data in figure 2 of Wunsch & Kerstein 2005), and some experiments indicate a slight decrease for $Pr \gtrsim 1$ (Ahlers *et al.* 2009). There are, however, experiments showing a very mild increase of Nu with increasing Pr (Ahlers *et al.* 2009).

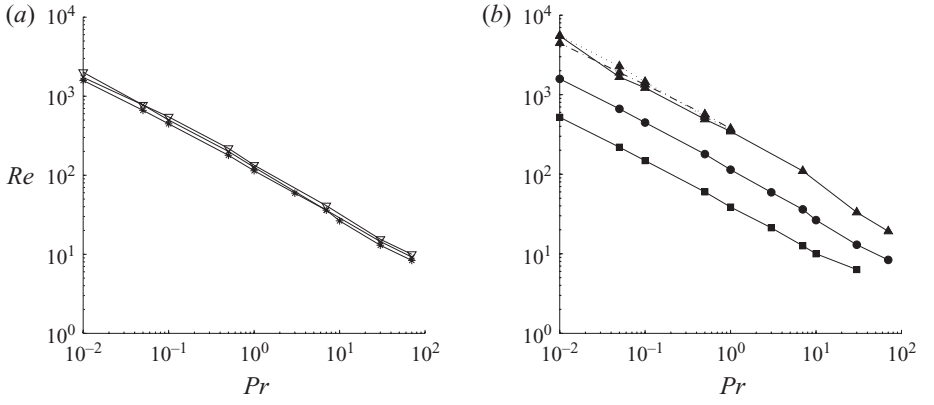

FIGURE 17. Effect of Pr on Re. Parameter values and layout of the figure are the same as in figure 15. ODT simulations show that $Re \sim Ra^{0.43} R_\rho^{-0.15} Pr^{-0.58\pm0.03}$.

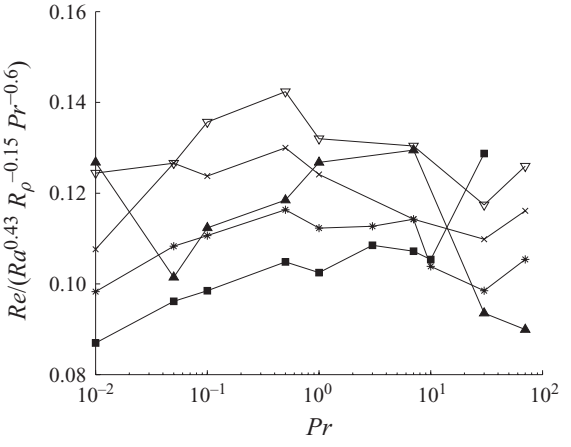

FIGURE 18. Re correlation obtained for $C = 10$ and $Z = 1$. Parameter values are the same as in figure 15.

A power-law dependence of Re on Pr can be seen in figure 17. We obtain the following correlation:

$$Re \sim Ra^{0.43} R_\rho^{-0.15} Pr^{-0.58\pm0.03}, \quad \text{when } Pr = 0.01\text{–}100, \tag{3.7}$$

with an average (maximum) deviation of the data of 9 % (30 %). The fitting of the data by (3.7) can be seen in figure 18 for $C = 10$ and $Z = 1$. The sensitivity of the exponents of Ra and R_ρ in (3.7) to C and Z is not explored here. Notice that these exponents are consistent with those in (3.4).

The turbulent kinetic energy equation is used next to show that (3.7) is consistent with (3.3) and (3.6). In a quasi-steady flow with no background shear and the present boundary conditions, the turbulent kinetic energy equation becomes

$$\langle\langle\varepsilon\rangle_z\rangle_t \sim g(\beta_T F_T - \beta_S F_S), \tag{3.8}$$

after temporally and spatially averaging (along $0 \leqslant z \leqslant h$) its terms. By taking $\langle\langle\varepsilon\rangle_z\rangle_t \sim U^3/L$, where U and L are respectively the velocity and length scales, we

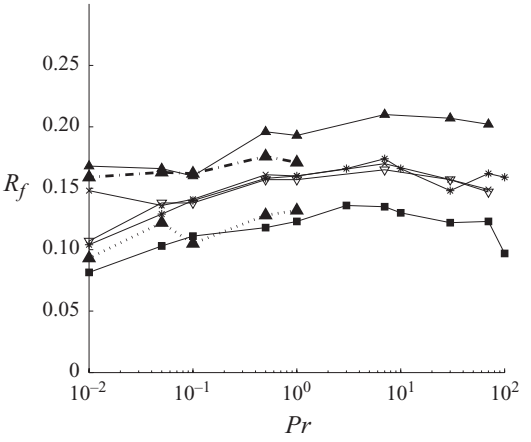

FIGURE 19. Effect of Pr on R_f. Parameter values and layout of the figure are the same as in figure 15.

obtain

$$Re^3 \sim RaNuPr^{-2}(1 - R_f), \tag{3.9}$$

after using $U \sim (\langle\langle TKE\rangle_z\rangle_t)^{1/2}$ and $L \sim h$. Parallel but more rigorous derivations of (3.9) are given in Ahlers *et al.* (2009) for 3D Rayleigh–Bénard convection and in Wunsch & Kerstein (2005) for the ODT analogue of this form of convection. Notice in figure 19 that the buoyancy ratio R_f is approximately constant over the ranges of Pr and other parameters considered. Thus, the term $(1 - R_f)$ is assumed constant. By inserting (3.3) into (3.9) we obtain $Re \sim Ra^{0.46} R_\rho^{-0.12} Pr^{-0.66}$, while by using (3.6) with (3.9) we obtain $Re \sim Ra^{0.44} R_\rho^{-0.1} Pr^{-0.59}$. Here the ranges of the exponents have been dropped for clarity. These last two expressions are close to (3.7).

Mixing-length theory of thermal convection gives for $Pr \gtrsim 0.1$ the scaling relationships $Nu \sim Ra^{1/3}$, i.e. Nu is independent of Pr and $Re \sim Ra^{4/9} Pr^{-2/3}$, while for $Pr \lesssim 0.1$ it suggests $Nu \sim Ra^{1/3} Pr^{1/3}$ (Siggia 1994). The last expression can also be obtained with dimensional analysis by assuming that the heat flux F_T is independent of h, as explained before, and is also independent of viscosity, since $\nu \ll \kappa_T$. These scaling relationships are not the same as (3.3)–(3.7), but may be close enough for rough calculations.

3.6. *Effect of Le*

The effect of Le on Nu predicted by ODT simulations and by the theory of Linden & Shirtcliffe (1978) is shown in figure 20. ODT data with the following parameters are considered here: $R_\rho = 1.25,\ 2,\ 4,\ 6$; $Ra = 10^8$; $Pr = 7$; $Le = 10^{-3}$–10^{-1}; $C = 10$; and $Z = 1,\ 100$. Figure 20 shows that simulations and theory predict a decrease of Nu when $Le \to 1$, and that this decrease starts at lower values of Le in more stable interfaces (larger R_ρ). Similar trends can be seen in figure 21 for Re. These decreases of Nu and Re occur because the mechanism producing thermal motions is suppressed when $Le \to 1$ and this suppression becomes active at lower Le in more stable interfaces. Figure 20 indicates that, as Le decreases, simulations and theory predict a decreasing sensitivity of Nu to Le. Figure 21 shows a similar behaviour for Re. The implication is that the diffusion of heat is so much larger than that of salt that the latter has no effect on thermal convection anymore. Interestingly, while the model of Linden & Shirtcliffe (1978) gives a monotonic variation of Nu as Le

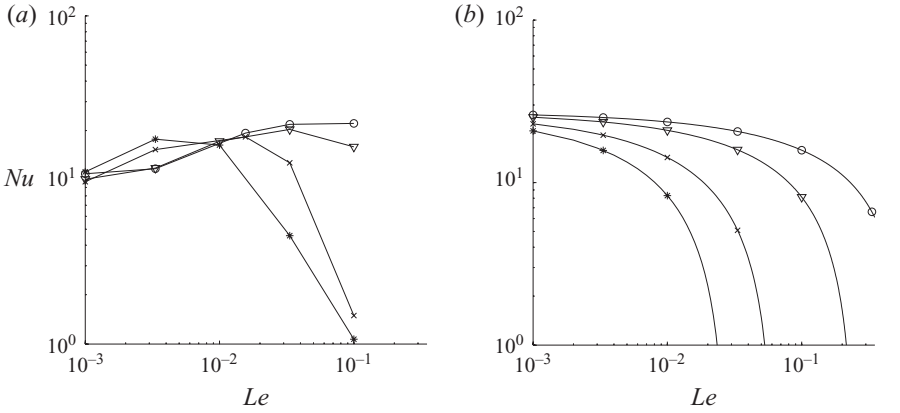

FIGURE 20. Effect of Le on Nu for $R_\rho = 1.25$ (circles), 2 (inverse triangles), 4 (crosses) and 6 (asterisks). (a) Simulation results for $Ra = 10^8$, $Pr = 7$, $C = 10$ and $Z = 1$. (b) Results from the theory by Linden & Shirtcliffe (1978).

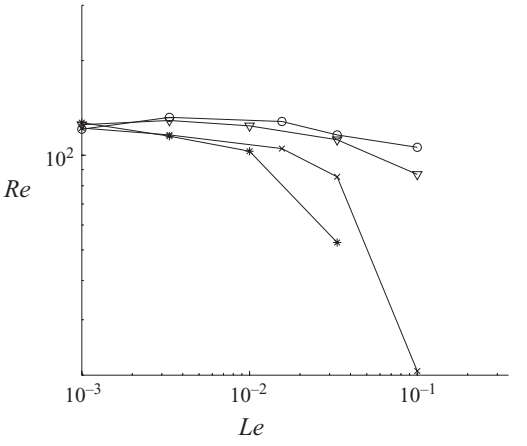

FIGURE 21. Effect of Le on Re predicted by ODT simulations. Parameter values of the simulations are the same as in figure 20(a).

decreases, ODT simulations show a non-monotonic behaviour. It is plausible that the double-diffusive interface exhibits more complicated behaviour than that predicted by the model of Linden & Shirtcliffe (1978), but independent confirmation of the behaviour indicated by ODT is needed to verify its validity. The foregoing trends, as well as the following ones on the effect of Le on R_f, were also observed with $Z = 100$.

Figure 22(a) shows the effect of Le on R_f predicted by ODT simulations at various R_ρ, and that measured by Turner (1965), Shirtcliffe (1973) and Takao & Narusawa (1980) for the constant-R_f regime. The experiments of Turner (1965) are bottom-heated experiments for the heat/salt system ($Le = 0.01$); Shirtcliffe (1973) uses the rundown configuration and the salt/sugar system ($Le = 0.33$) and Takao & Narusawa (1980) uses the bottom-heated configuration with three types of aqueous solutions ($Le = 0.02$, 0.01, 0.003). Also shown in figure 22(a) is the relationship $R_f = Le^{1/2}$, which is obtained by Linden & Shirtcliffe (1978) and found to be a lower bound for R_f by Stern (1982) (cf. § 3.2). Notice in figure 22(a) that ODT results for $R_\rho = 4$ and 6 are in the constant-R_f regime. For this regime, figure 22(a) shows that the

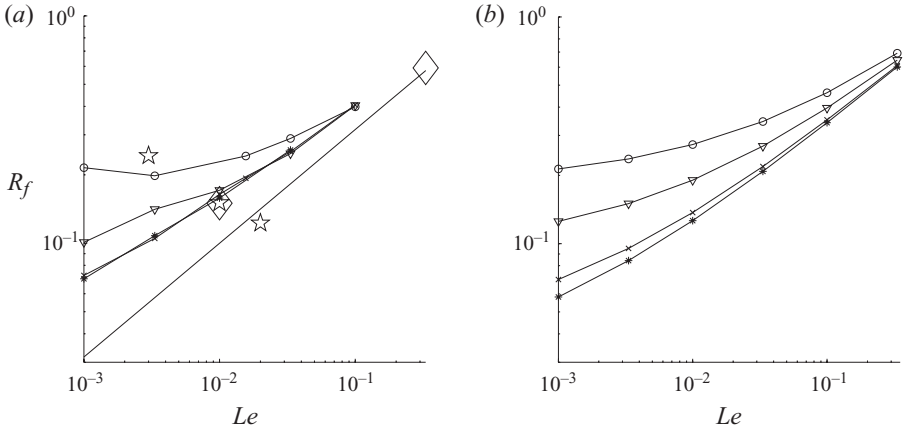

FIGURE 22. Effect of Le on R_f. Parameter values are the same as in figure 20(a). (a) Simulation results. (b) Results from the theory by Linden (1974). Also shown in (a) are results for the constant-R_f regime from the experiments by Turner (1965) and Shirtcliffe (1973) (diamonds), and those by Takao & Narusawa (1980) (stars), as well as the relationship $R_f = Le^{1/2}$ (unmarked solid line), explained in the text. For the constant-R_f regime, ODT simulations agree better with the experiments by Turner (1965) and Shirtcliffe (1973) than with those by Takao & Narusawa (1980).

simulation results agree better with the experiments by Turner (1965) and Shirtcliffe (1973) than with those by Takao & Narusawa (1980). This is also supported by ODT results with $Z = 100$ (not shown). By fitting a power law to the simulation results in the constant-R_f regime, we obtain $R_f \sim Le^{0.41\pm0.04}$, where the range in the exponent denotes its sensitivity to Z. It can also be seen in figure 22(a) that, for fixed Le, ODT results for R_f in the constant-R_f regime are larger than $R_f = Le^{1/2}$. This is consistent with a variational analysis showing that this expression represents a lower bound for R_f (Stern 1982).

Figure 22(a) generalizes, to a range of Le values, the results of figure 5 indicating that ODT predictions of R_f for $R_\rho = 1.25$ and 2 are larger than those in the constant-R_f regime, for given Le. This happens because at these lower values of R_ρ the interface is heavily eroded by eddies enhancing the transport of salt, as discussed in § 3.2. Notice in figure 22(b) that the theory of Linden (1974) predicts a similar behaviour, including increasing R_ρ sensitivity as Le decreases.

4. Sheared interfaces

The effect of background shear on the heat and salt fluxes is discussed in this section. The following parameters are considered: $Ri \approx 10^{-4}$–10^4, $R_\rho = 1.1$–6, $Ra = 10^7$–10^9, $Pr = 7$, $Le = 0.01$, $C = 1, 10$ and $Z = 0.01, 1, 100$. We will compare ODT results with those from a Reynolds stress model (Canuto *et al.* 2008*a*) and with stirring experiments (Atkinson 1994). This comparison is qualitative and is not used to validate our results since molecular processes are unresolved in Reynolds stress models, while they are fully resolved in ODT, and grid-stirred turbulence differs from shear-induced turbulence (Turner 1979). We start by giving a description of the flow in § 4.1, then describe briefly the model by Canuto *et al.* (2008*a*) and finish by presenting our simulation results in § 4.3.

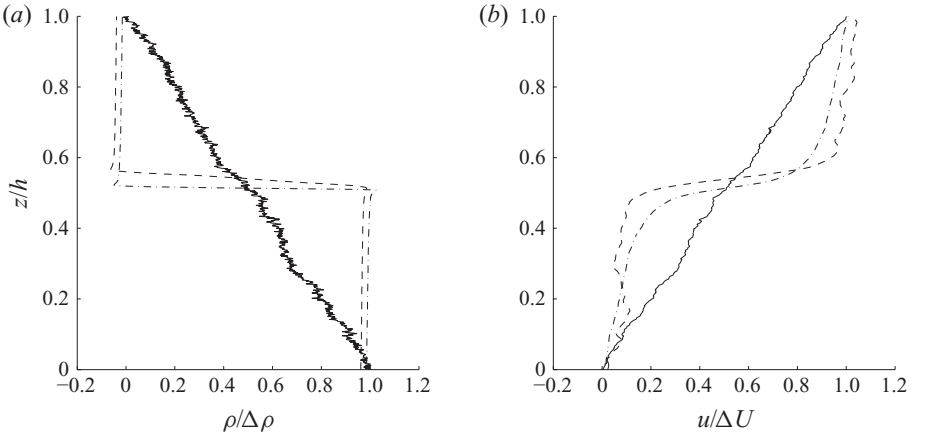

FIGURE 23. Effect of Ri on (a) the time-averaged density $\rho/\Delta\rho$ and (b) horizontal velocity $u/\Delta U$ profiles. Parameter values are $Ri = 794$ (dashed lines), 7.94 (dash-dotted lines), 0.1 (solid lines), and $R_\rho = 6$, $Ra = 10^8$, $Le = 0.01$, $Pr = 7$, $C = 10$ and $Z = 1$.

4.1. *Flow description*

Figure 23(a) shows that when the background shear is not too high (Ri is high enough), the characteristic structure of the double-diffusive interface, cf. § 3.1, is preserved, and the shape of the horizontal velocity profile resembles that set initially, cf. § 2.5. Also, as long as the shear is not too high, the eddy erosion of the double-diffusive interface becomes more aggressive as the shear level increases (Ri decreases), as can be seen in figures 24(a), 24(b) and 24(c) where the interface is at $z/h \approx 0.5$. Notice in figure 24(c) that some eddies penetrate into the interface. Consequently, a shear increase leads to a sharpening of the density gradient at the interface, cf. figure 23(a). These observations are similar to those discussed in § 3.2 on the effect of the stability parameter R_ρ. Eventually, when the background shear is high enough (Ri is low enough), the interface is broken, cf. figure 24(d), and the density and horizontal velocity profiles become linear, cf. figure 23. Smaller eddies can be seen at this high level of shear in figure 24(d), where $Re = O(10^3)$, in comparison with those at lower levels of shear in figures 24(a), 24(b) and 24(c), where $Re = O(10^2)$.

4.2. *Reynolds stress model of Canuto* et al. *(2008a)*

The Reynolds stress model of Canuto *et al.* (2008a) gives algebraic relationships between the dimensionless heat and salt fluxes and their governing parameters. Within this framework the effects of pressure and molecular processes are modelled. The dimensionless heat and salt fluxes are represented by

$$\Gamma_h = \Gamma_h(R_\rho, Ri), \quad R_f = R_f(R_\rho, Ri), \tag{4.1}$$

where the heat mixing efficiency Γ_h is defined by

$$\Gamma_h = -\frac{N^2}{\langle\varepsilon\rangle_V}\frac{F_T}{\Delta T/h}, \tag{4.2}$$

where $N^2 = -g(\Delta\rho/\rho_0)/h$, and $\langle\rangle_V$ denotes a volumetric average. The definitions of Γ_h, R_ρ, Ri and N^2 are based on the vertical gradients of u, ρ/ρ_0, T and S averaged over some appropriate vertical length scale, much larger than those associated with molecular processes. Here these gradients become $\Delta U/h$, $(\Delta\rho/\rho_0)/h$, $\Delta T/h$ and $\Delta S/h$ when averaged along $0 \leqslant z \leqslant h$.

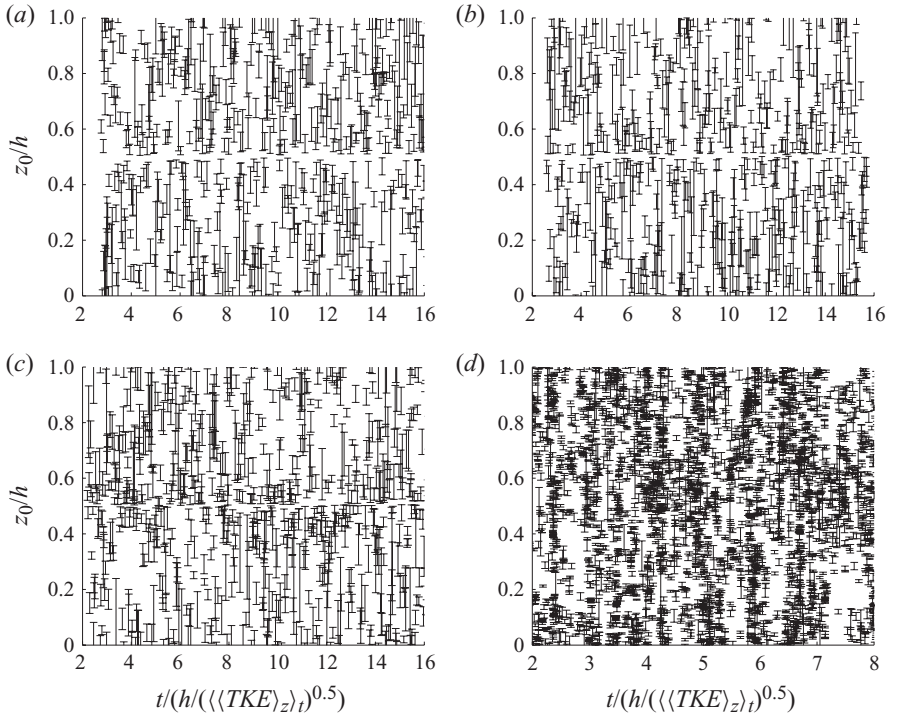

FIGURE 24. Temporal sequence of the locations z_0 and sizes l (vertical bars) of eddy events generated in an ODT simulation of double-diffusive convection with background shear. For clarity, not every eddy event implemented in the simulations is shown. Values of Ri are (a) ∞, (b) 794, (c) 7.94 and (d) 0.1. Other parameter values are $R_\rho = 6$, $Ra = 10^8$, $Le = 0.01$, $Pr = 7$, $C = 10$ and $Z = 1$.

In the model by Canuto *et al.* (2008*a*) the governing equations for $u_i = (u, v, w)$, T and S are the Navier–Stokes equations with the Boussinesq approximations. The flow properties are decomposed into mean and fluctuating parts, i.e. $s = \langle s\rangle + s'$, where $s = u_i, T, S$, and $\langle s\rangle$ and s' denote the mean and fluctuating components of s, respectively. This decomposition is substituted into the governing equations. Further algebraic manipulation gives a set of governing equations for the second-order moments $\langle u_i' u_j'\rangle$, $\langle u_i' T'\rangle$, $\langle u_i' S'\rangle$, $\langle T'^2\rangle$, $\langle S'^2\rangle$ and $\langle T' S'\rangle$. Of main interest are the moments $\langle w' T'\rangle$ and $\langle w' S'\rangle$ representing the vertical heat and salt fluxes, respectively. The governing equation for any second-order moment ψ has the form

$$\frac{\mathrm{D}\psi}{\mathrm{D}t} = \mathscr{S} + \mathscr{D} + \mathscr{P} - \tau_\psi^{-1}\psi. \tag{4.3}$$

Here $\mathscr{S}$ represents the source or sink terms that can be calculated directly, i.e. without modelling, $\mathscr{D}$ is a turbulent diffusion term containing third-order moments, $\mathscr{P}$ contains certain terms arising from pressure/turbulence interactions and $-\tau_\psi^{-1}\psi$ represents the combined effect of dissipation by molecular processes and the return-to-isotropy induced by pressure, with τ_ψ being a relaxation–dissipation time scale for the moment ψ. The terms $\mathscr{D}$, $\mathscr{P}$ and τ_ψ require further modelling. The modelling of $\mathscr{P}$ and τ_ψ is described in Canuto *et al.* (2001). By assuming $\mathscr{D} = 0$, quasi-steady-state conditions, and neglecting all gradients except those in the vertical direction z, a set of algebraic linear equations for the second-order moments are obtained. The model

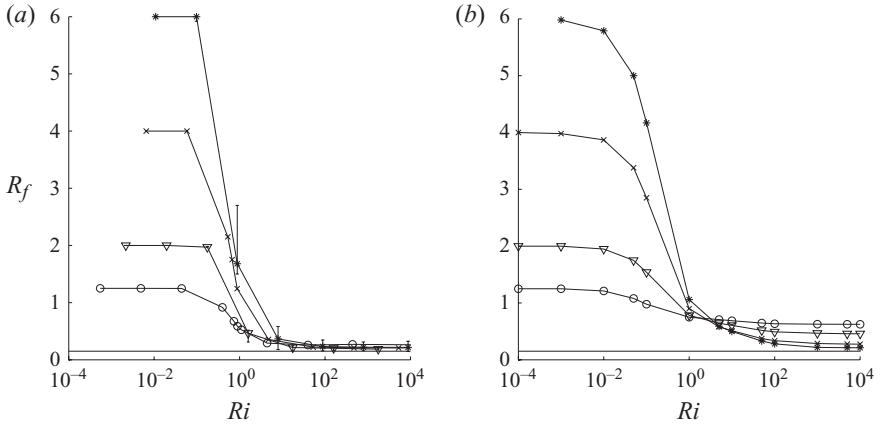

FIGURE 25. Effect of Ri on R_f. (a) Simulation results. (b) Results from Canuto *et al.* (2008*a*). Parameter values are $R_\rho = 1.25$ (circles), 2 (inverse triangles), 4 (crosses), 6 (asterisks), and $Ra = 10^8$, $Le = 0.01$, $Pr = 7$, $C = 10$ and $Z = 1$. The sensitivity of the results to C and Z, defined in the text, is denoted with error bars in (a) for $R_\rho = 2$ and 6. The horizontal line denotes the value of $R_f = 0.15$ found in experimental studies of unsheared double-diffusive interfaces (Turner 1965). A transition between two flow regimes occurs near $Ri \sim 1$.

is completed with an expression for the time scales τ_ψ. These time scales have usually been treated as adjustable constants. The key contribution of Canuto *et al.* (2008*a*,*b*) is to express the relaxation–dissipation time scales of the heat and salt fluxes as functions of R_ρ and Ri based on the following physical arguments: these time scales are damped (reduced) in strongly stratified environments, which introduces the effect of Ri, and such damping is counteracted by thermal convection in double diffusion, introducing the effect of R_ρ.

The heat mixing efficiency Γ_h and the flux ratio R_f are direct outputs of the model by Canuto *et al.* (2008*a*). They are obtained by solving iteratively the algebraic equations (13*a*)–(13*c*), (14), (16*c*), (A1)–(A4) and (B1)–(B6) of Canuto *et al.* (2002), but with (B1) replaced with (4*l*) of Canuto *et al.* (2008*a*). With this replacement, the relaxation–dissipation time scales of the heat and salt fluxes are not adjustable constants but functions of R_ρ and Ri.

4.3. *Effect of Ri*

The effect of Ri on R_f is shown in figures 25 and 26. These figures show the predictions by both ODT and the model by Canuto *et al.* (2008*a*). Hereinafter this model is referred to as C8. The symbols in all the figures in § 4.3 (figures 25–33) denote the data obtained from ODT, C8 or experiments, and the curves in these figures are made by connecting the symbols with line segments. The error bars in figure 25(a) denote the range of variation of R_f when C and Z are varied and other parameters are held constant. The ODT curves in figure 25(a) are for $C = 10$ and $Z = 1$. The variations shown by these error bars suggest that the trends shown in figure 25 are insensitive to the model parameters. Such trends were also observed to be insensitive to Ra (not shown).

Notice in figures 25 and 26 the large variation of R_f with $Ri \sim 1$. This variation is seen to be more abrupt in ODT results than in predictions by C8. When Ri lies outside the transition region near $Ri \sim 1$, figures 25 and 26 show that it has no effect on R_f, according to both ODT and C8. Also, notice in figure 27 that for $Ri \gg 1$, results from ODT simulations agree better with the limit $Ri = \infty$, shown in this figure

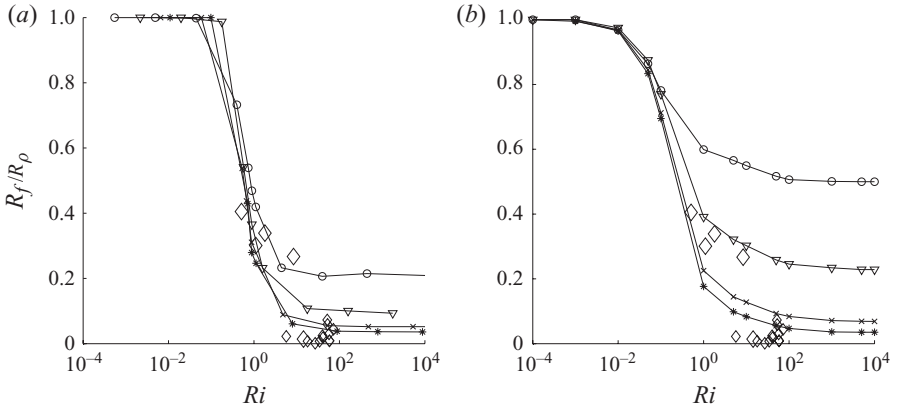

FIGURE 26. Effect of Ri on R_f/R_ρ. Parameter values and layout of the figure are the same as in figure 25. Also shown are the experimental results from Atkinson (1994) for $R_\rho = 1.48$, 2.26, 2.39, 3.33 and 4.97 (large diamonds), in order of increasing Ri_{st}, as well as those for $R_\rho = 17.9$–437 (small diamonds). For the experimental data, the abscissa represents Ri_{st}, defined in the text.

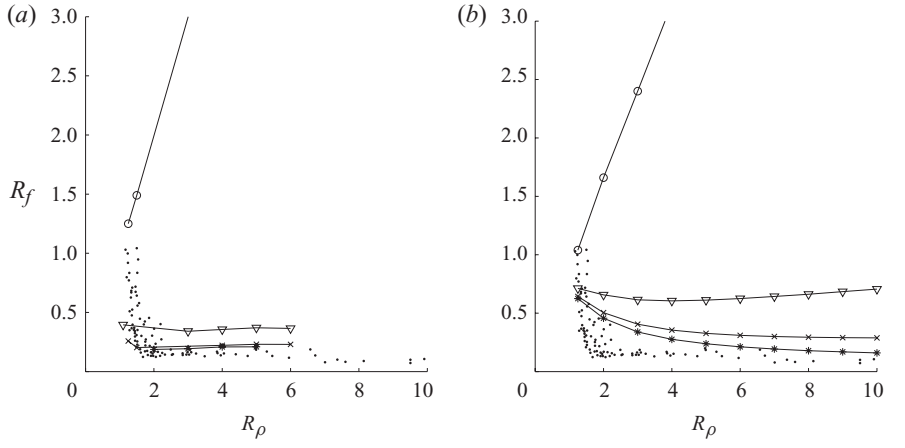

FIGURE 27. Effect of R_ρ on R_f. (*a*) Simulation results. (*b*) Results from Canuto *et al.* (2008*a*). Parameter values for the simulations are $Ri = 0.04$–0.1 (circles), 1.8–8.0 (inverse triangles), 40–88 (crosses), 1800–7000 (asterisks), and $Ra = 10^8$, $Le = 0.01$, $Pr = 7$, $C = 10$ and $Z = 1$. Input values for the theory are $Ri = 0.07$ (circles), 4 (inverse triangles), 65 (crosses) and 4500 (asterisks). Experimental results for unsheared interfaces compiled by Kelley (1990) are also shown (dots).

using experimental data of unsheared interfaces, than results from C8. The latter results are seen to be insensitive to Ri when $Ri \gtrsim 4500$.

In grid-stirring experiments of double-diffusive interfaces a warm layer of saline water is set under a layer of cold fresh water in an insulated tank, i.e. a rundown configuration is used, with a pair of oscillating grids at the centre of each layer (Crapper 1976; Atkinson 1994). The turbulence induced by stirring a grid in a fluid with no density stratification is characterized by a velocity scale u_{st} and a length scale l_{st}. Using these scales a Richardson number can be defined as $Ri_{st} = g(\Delta\rho/\rho_0)l_{st}/u_{st}^2$. Only the data of Atkinson (1994) are used here since Crapper (1976) does not give enough information to calculate Ri_{st}. In the experiments of Atkinson (1994) the

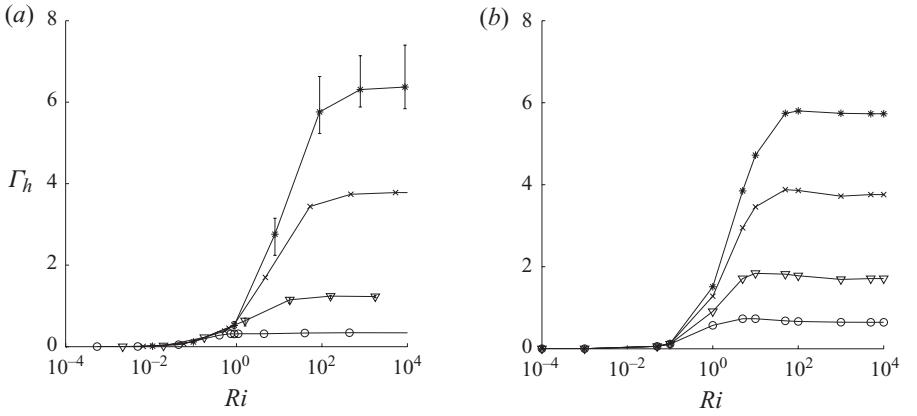

FIGURE 28. Effect of Ri on the heat mixing efficiency Γ_h. Parameter values, layout of the figure and definition of the error bars in (a) are the same as in figure 25.

Richardson number Ri_{st} is varied by holding u_{st} and l_{st} approximately constant and by varying R_ρ in the range $R_\rho = 1.5$–437. Figure 26 shows that the transition region predicted by ODT and C8 for double diffusion with background shear is also observed in the grid-stirring experiments by Atkinson (1994). In figure 26 the abscissa represents Ri_{st} for the experimental data.

Figure 28 shows how the heat mixing efficiency Γ_h varies with Ri according to both ODT simulations and C8. The error bars in figure 28(a) are defined as in figure 25(a). The effects of the model parameters on this variation were observed to be small. Also the effect of Ra on such variation was seen to be small (not shown). Figure 28 shows that ODT and C8 give a similar variation of Γ_h with Ri. However, as seen before for R_f, there is some discrepancy when $Ri \gg 1$, where ODT predicts smaller values of Γ_h, cf. figure 28.

So far, in this section, results from ODT simulations have been compared with those from C8 and experiments. Next, ODT results are used to discuss in more depth the effect of Ri on the fluxes of heat and salt.

For values of $Ri \ll 1$, figure 26 shows that $R_f = R_\rho$. This result suggests that the same mechanism is transporting the heat and salt. Moreover, figure 29 indicates that when $Ri \ll 1$, the production of turbulent kinetic energy (TKE) by the mean shear, $P_U = -\langle u'w' \rangle \Delta U / h$, is dominant in comparison with the production of TKE by the temperature field, $P_T = g\beta_T F_T$, and its destruction by the salinity field, $D_S = g\beta_S F_S$. Therefore, the mechanism transporting the heat and salt is the turbulence induced by the background shear. The shapes of the curves in figure 29, which are for $R_\rho = 4$, are observed to be representative of the range $R_\rho = 2$–6 (not shown). On the other hand, figures 25 and 27 show that when $Ri \gg 1$, the variation of R_f with R_ρ resembles that seen in unsheared interfaces, suggesting that the process of double-diffusive convection is dominant. This observation is supported by figure 29, which shows that for $Ri \gg 1$, the turbulent fluctuations are mainly produced by the temperature field.

In the transition region near $Ri \sim 1$, an increase of shear (decrease of Ri) enhances the vertical transport of salt and heat, since it increases both R_f and Nu, as can be seen, respectively, in figures 25 and 30. Figure 30 shows the effect of Ri on Nu according to both ODT and C8. The values of Nu from C8 are calculated with $Nu = -\Gamma_h \langle \varepsilon \rangle_V / (N^2 \kappa_T)$, which is obtained using (1.2) and (4.2). For this calculation,

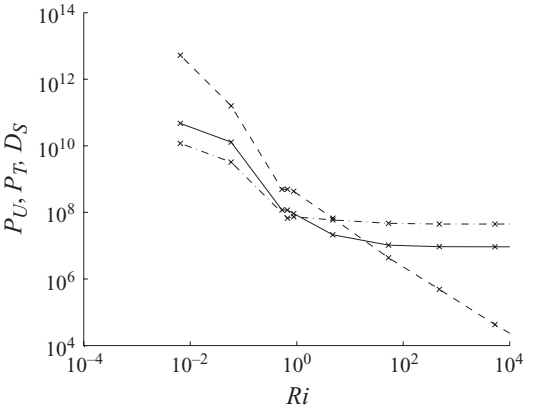

FIGURE 29. Effect of Ri on the production of turbulent kinetic energy by the mean shear, $P_U = -\langle u'w'\rangle \Delta U/h$ (dashed line), and by the temperature field, $P_T = g\beta_T F_T$ (dash-dotted line), and its destruction by the salinity field, $D_S = g\beta_S F_S$ (solid line). These terms are made dimensionless using h as a length scale and h^2/ν as a time scale. Shown are the results from ODT simulations for $R_\rho = 4$, $Ra = 10^8$, $Le = 0.01$, $Pr = 7$, $C = 10$ and $Z = 1$.

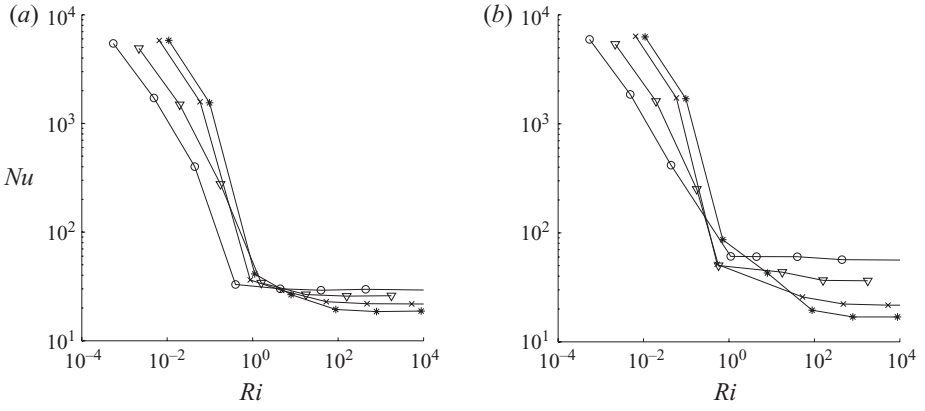

FIGURE 30. Effect of Ri on Nu. Parameter values and layout of the figure are the same as in figure 25.

we use the results in figure 28(b) for Γ_h and values of $\langle\varepsilon\rangle_V/(N^2\kappa_T)$ from ODT simulations, with $\langle\varepsilon\rangle_V = \langle\langle\varepsilon\rangle_z\rangle_t$, cf. § 2.6.

The enhancement of the fluxes near $Ri \sim 1$ with decreasing Ri can be seen to occur in two steps: one gradual and the other abrupt. Consider first a decrease of Ri from, say, 10^2 to 10. The eddy erosion on the interface becomes more aggressive, cf. figures 24(a), 24(b) and 24(c) for example. Figures 25(a) and 30(a) show that the salt and heat fluxes increase slightly. Figure 29 indicates that the production of turbulent fluctuations from background shear P_U starts to become important. Figure 29 also shows that the damping of fluctuations by the salinity field D_S, which is constant when $Ri \gg 1$, starts to increase, while the contribution by the temperature field to the turbulent kinetic energy P_T remains constant. Thus, the fluctuations induced by shear start to mix the salt, but their effect on P_T is small. On the other hand, once the value of P_U is large enough in comparison with P_T, as occurs near $Ri \approx 1$ in figure 29 for $R_\rho = 4$, P_T starts to be affected by the background shear and increases sharply

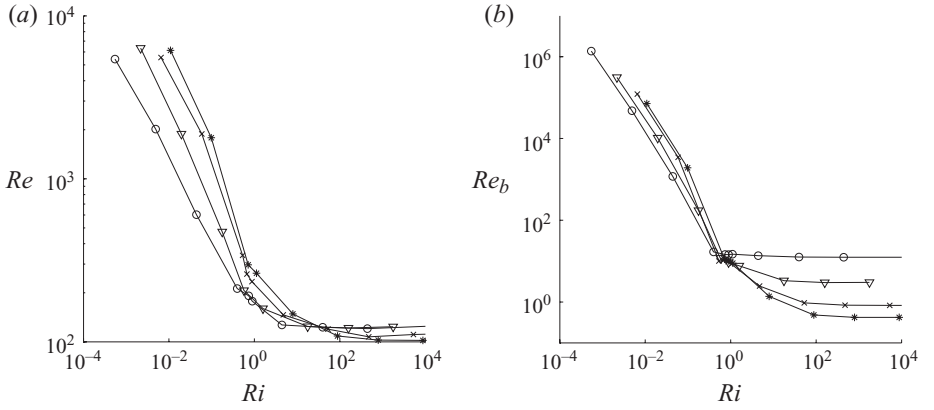

FIGURE 31. Effect of Ri on (a) Re and (b) buoyancy Reynolds number Re_b defined as $Re_b = \langle\langle\varepsilon\rangle_z\rangle_t/(\nu N^2)$. Parameter values are the same as in figure 25.

with decreasing Ri. At this point the turbulent fluctuations induced by shear are high enough to break the double-diffusive interface, cf. figure 24(d) for example. A further decrease of Ri leads to a drastic increase of the fluxes of heat and salt, cf. figures 25 and 30.

The variation of the turbulence intensity with Ri resembles that described for Nu. This can be seen in figures 31(a) and 31(b), where the turbulence intensity is represented respectively by Re, as done throughout the present work, and by a buoyancy Reynolds number Re_b defined as $Re_b = \langle\langle\varepsilon\rangle_z\rangle_t/(\nu N^2)$, which is commonly used by oceanographers (e.g. Gargett 1989). The turbulence intensity cannot be analysed in this way with C8.

Figure 32(a) shows that when $Ri \ll 1$, the heat flux scales as $Nu \sim \Delta U h/\nu$, in agreement with the previous finding that the transport of heat is dominated by shear-induced turbulence. On the other hand, notice in figure 32(a) the large scatter of the data when using this scaling for $Ri \gg 1$. Such scatter is reduced by assuming $Nu \sim (Ra/R_\rho)^{0.36}$, cf. § 3.3, as can be seen in figure 32(b). This agrees with the previous observation that the transport of heat is dominated by double-diffusive convection when $Ri \gg 1$. Notice also in figure 32(c) that the scaling Nu/Re collapses the data for all values of Ri, though there is some scatter when $Ri \gg 1$. The normalization of the heat flux shown in figure 32 highlights a transition near $Ri \sim 1$ between a shear-dominated and a double-diffusion-dominated regime.

We remark that a Richardson number defined as $Ri_g = -g(\partial(\rho/\rho_0)/\partial z)/(\partial u/\partial z)^2$, with the gradients evaluated at the interface, is within the same order of magnitude of Ri, cf. figure 33. This is useful since Ri is easier to measure.

5. Summary and conclusions

The present work is a parametric study of the heat and salt fluxes across double-diffusive interfaces. It employs one-dimensional-turbulence simulations to determine the scaling of these fluxes with the governing parameters. Both unsheared and sheared interfaces are considered by using jump-periodic boundary conditions. Key distinctions of this work are the consideration of a very broad parameter space and the analysis of fully resolved sheared double-diffusive interfaces.

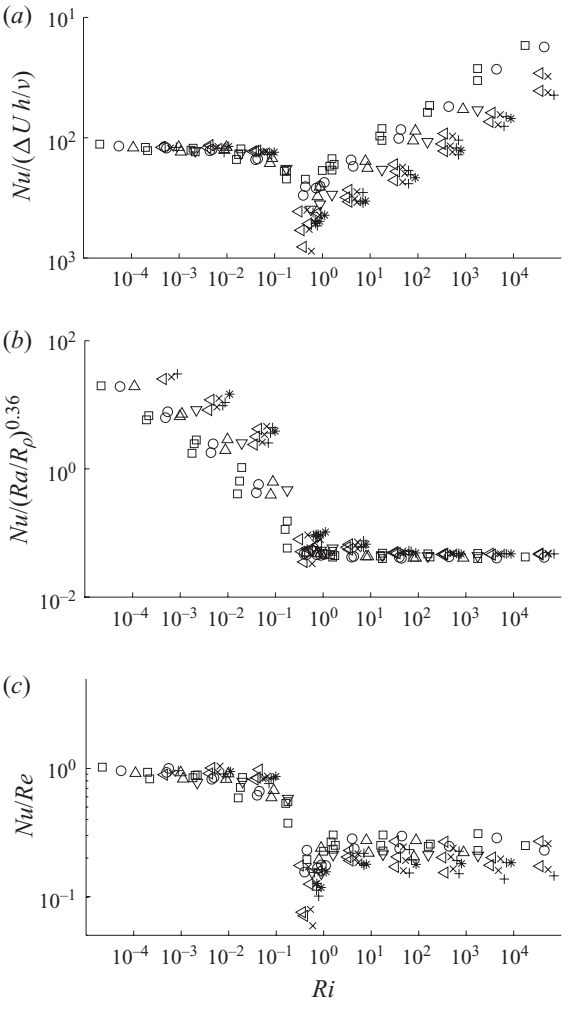

FIGURE 32. Effect of Ri on the rescaled heat flux. Parameter values are $R_\rho = 1.1$ (squares), 1.25 (circles), 1.5 (triangles), 2 (inverse triangles), 3 (left triangles), 4 (crosses), 5 (plus signs), 6 (asterisks); $Le = 0.01$, $Pr = 7$, $C = 10$ and $Z = 1$. Results for $Ra = 10^7$, 10^8 and 10^9 are shown. The scaling $Nu/(\Delta U h/\nu)$ in (a) highlights a shear-turbulence-dominated regime for $Ri \ll 1$, and the scaling $Nu/(Ra/R_\rho)^{0.36}$ in (b) highlights a double-diffusive-convection-dominated regime for $Ri \gg 1$. Notice in (c) that the scaling Nu/Re collapses the data for all values of Ri, though there is some scatter when $Ri \gg 1$.

Simulations of unsheared interfaces with $R_\rho = 1.05$–6, $Ra = 10^6$–10^{10} and $Le = 0.01$ show that

$$Nu \sim \begin{cases} (Ra/R_\rho)^{0.37\pm0.03} & \text{when } Pr = 3\text{–}100 \\ (Ra/R_\rho)^{0.31}\, Pr^{0.22\pm0.04} & \text{when } Pr = 0.01\text{–}1, \end{cases} \tag{5.1}$$

$$Re \sim Ra^{0.45\pm0.04} R_\rho^{-0.12\pm0.05} Pr^{-0.58\pm0.03} \quad \text{when } Pr = 0.01\text{–}100. \tag{5.2}$$

A slight decrease of Nu with Pr is seen when $Pr \approx 10$–100, but it is not quantified since it is too small to accurately fit the available data. The sensitivity of the exponents to the model parameters C and Z is denoted above with ranges. ODT simulations also show that R_f stays approximately constant as Pr is varied, and that R_f increases

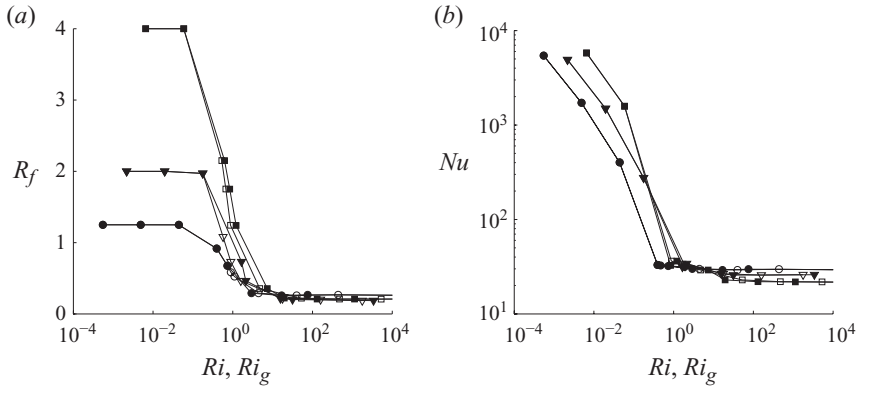

FIGURE 33. Effect of Ri (open symbols) and Ri_g (solid symbols) on (*a*) R_f and (*b*) Nu for $R_\rho = 1.25$ (circles), 2 (inverse triangles) and 4 (squares). Parameter values are the same as in figure 25.

slightly with Ra when R_ρ is low, i.e. when the interface is unstable, and that this tendency is reduced for increasing R_ρ. The above scaling of Nu with Ra/R_ρ is also observed for $Pr = 7$ when a rundown configuration is used. Nonetheless, in general, some sensitivity of the exponents of the identified correlations to the boundary conditions is expected. This sensitivity could be explored in future studies.

Interestingly, Ra/R_ρ appears as a dominant parameter for Nu in the above correlations, as a result of least-squares minimization. Ra/R_ρ can be seen as a ratio of destabilizing and stabilizing effects. To our knowledge, the above scalings between Nu and Ra are, together with those by Marmorino & Caldwell (1976), $Nu \sim Ra^{0.37\pm0.1}$ for $Ra \sim 10^{10}$–10^{11} and $Pr \approx 7$ (cf. Kelley *et al.* 2003), the only ones obtained for double-diffusive convection in the diffusive regime by means other than dimensional reasoning.

Regarding the effect of Le in unsheared interfaces, ODT simulations for $Pr = 7$ and $Le = 10^{-3}$–10^{-1} show that $Nu \to 0$ when $Le \to 1$, as the double-diffusive convection is suppressed, and that Nu approaches an approximately constant value when Le decreases in the range 10^{-3}–10^{-1}, since the diffusion of salt becomes small enough for it not to have an effect on thermal convection. Similar trends are indicated by the model of Linden & Shirtcliffe (1978). However, while this model shows that Nu monotonically approaches an approximately constant value, the simulations show a more complex non-monotonic behaviour. In stable interfaces ($R_\rho = 4$ and 6), R_f is observed to scale as $R_f \sim Le^{0.41\pm0.04}$. This result is important because of a previous discrepancy among experiments. The scaling exhibited by ODT agrees better with the experiments by Turner (1965) and Shirtcliffe (1973) than with those by Takao & Narusawa (1980). In unstable interfaces ($R_\rho = 1.25$ and 2), R_f deviates from this scaling relationship, as the erosion of the interface becomes important. Such a behaviour is also indicated by the model of Linden (1974).

Three flow regimes are observed in ODT simulations of sheared interfaces with $Pr = 7$ and $Le = 0.01$. When $Ri \ll 1$, shear-induced mixing dominates, the interface is broken and the fluxes are given by $Nu \sim \Delta U h/\nu$ and $R_f = R_\rho$. Near $Ri \sim 1$, a transition region occurs. In this region the heat and salt fluxes increase as the shear increases (Ri decreases). This agrees with the observations in the ocean of double-diffusive interfaces (Padman 1994) but contrasts with the observations in salt-fingering interfaces, where the fluxes appear to be damped by background turbulence (Linden

1971; St. Laurent & Schmitt 1999). Finally, when $Ri \gg 1$, double-diffusive convection dominates, the characteristic structure of the double-diffusive interface is preserved and the scaling of the fluxes resembles that in unsheared interfaces.

The transition region merits further study with experiments or DNS, in order to obtain an accurate estimate of the transition value of Ri and to explore the possible effect of interfacial waves on the fluxes, which cannot be captured with ODT. Although it has been argued that these waves would increase the fluxes by sharpening interfacial gradients (Linden & Shirtcliffe 1978, p. 428) and/or by breaking (Turner 1979, p. 275), visualizations of unsheared interfaces do not show the presence of such waves (Fernando 1989).

Overall, the agreement between ODT results for sheared interfaces and predictions by Canuto *et al.* (2008*a*) is satisfactory, though the latter predicts a less abrupt transition near $Ri \sim 1$, and higher values of R_f and Γ_H when $Ri \gtrsim 1$. These comparisons are important since models like that of Canuto *et al.* (2008*a*) are ultimately used in ocean circulation models. ODT can complement such models by providing information that is not otherwise available, including measures of turbulence intensity such as $Re(Ri, R_\rho)$, a relationship between bulk (Ri) and gradient (Ri_g) Richardson numbers, and transient effects. The accuracy of this information would be subject to ongoing evaluation as reliable comparison data become available.

A follow-up of the present study of a single double-diffusive interface could be that of a double-diffusive staircase. Although the former case is more fundamental, the latter is of more practical relevance. An unsheared double-diffusive staircase has already been simulated using a minimal ODT formulation that is not applicable to sheared interfaces (Kerstein 1999*b*). Future work could use the present formulation to simulate a sheared staircase and study the evolution of the interfaces, as well as the parametrization of the fluxes. Moreover, future studies should consider the effect of having a nonlinear equation of state for the fluid and determine if the phenomenon of interface migration is due to the nonlinearity of the equation of state for seawater (McDougall 1981; Kelley *et al.* 2003). In addition, future work could consider the regime $Pr < 0.01$, of importance in astrophysics (Chabrier & Baraffe 2007), and transient effects in the regime $R_\rho > 10$, of interest for the design of solar ponds (e.g. Newell 1984; Suárez, Tyler & Childress 2010).

This work was supported by the US Department of Energy, Office of Basic Energy Sciences, Division of Chemical Sciences, Geosciences, and Biosciences. Sandia National Laboratories is a multi-program laboratory operated by Sandia Corporation, a Lockheed Martin Company, for the US Department of Energy under contract DE-AC04-94-AL85000. Simulations were performed at Sandia National Laboratories on the Shasta Linux Cluster.

REFERENCES

Ahlers, G., Grossmann, S. & Lohse, D. 2009 Heat transfer and large scale dynamics in turbulent Rayleigh–Bénard convection. *Rev. Mod. Phys.* **81**, 503–537.

Ashurst, W. T. & Kerstein, A. R. 2005 One-dimensional turbulence: variable-density formulation and application to mixing layers. *Phys. Fluids* **17**, 025107.

Atkinson, J. F. 1994 Interfacial fluxes at a grid-stirred diffusive interface. *Intl J. Heat Mass Transfer* **37**, 2089–2099.

Canuto, V. M., Cheng, Y. & Howard, A. M. 2008*a* A new model for double diffusion plus turbulence. *Geophys. Res. Lett.* **35**, 2613.

Canuto, V. M., Cheng, Y., Howard, A. M. & Esau, I. N. 2008*b* Stably stratified flows: a model with no Ri(cr). *J. Atmos. Sci.* **65**, 2437–2447.

Canuto, V. M., Howard, A., Cheng, Y. & Dubovikov, M. S. 2001 Ocean turbulence. Part I. One-point closure model – momentum and heat vertical diffusivities. *J. Phys. Oceanogr.* **31**, 1413–1426.

Canuto, V. M., Howard, A., Cheng, Y. & Dubovikov, M. S. 2002 Ocean turbulence. Part II. Vertical diffusivities of momentum, heat, salt, mass, and passive scalars. *J. Phys. Oceanogr.* **32**, 240–264.

Chabrier, G. & Baraffe, I. 2007 Heat transport in giant (exo)planets: a new perspective. *Astrophys. J. Lett.* **661**, L81–L84.

Crapper, P. F. 1975 Measurements across a diffusive interface. *Deep Sea Res.* **22**, 537–545.

Crapper, P. F. 1976 Fluxes of heat and salt across a diffusive interface in the presence of grid generated turbulence. *Intl J. Heat Mass Transfer* **19**, 1371–1378.

Dreeben, T. D. & Kerstein, A. R. 2000 Simulation of vertical slot convection using one-dimensional turbulence. *Intl J. Heat Mass Transfer* **43**, 3823–3834.

Echekki, T., Kerstein, A. R., Dreeben, T. D. & Chen, J. Y. 2001 One-dimensional turbulence simulation of turbulent jet diffusion flames: model formulation and illustrative applications. *Combust. Flame* **125**, 1083–1105.

Fernando, H. J. S. 1989 Buoyancy transfer across a diffusive interface. *J. Fluid Mech.* **209**, 1–34.

Fernando, H. J. S. 1991 Turbulent mixing in stratified fluids. *Annu. Rev. Fluid Mech.* **23**, 455–493.

Funfschilling, D., Brown, E., Nikolaenko, A. & Ahlers, G. 2005 Heat transport by turbulent Rayleigh–Bénard convection in cylindrical samples with aspect ratio one and larger. *J. Fluid Mech.* **536**, 145–154.

Gargett, A. E. 1989 Ocean turbulence. *Annu. Rev. Fluid Mech.* **21**, 419–451.

Grossmann, S. & Lohse, D. 2000 Scaling in thermal convection: a unifying theory. *J. Fluid Mech.* **407**, 27–56.

Inoue, R., Yamazaki, H., Wolk, F., Kono, T. & Yoshida, J. 2007 An estimation of buoyancy flux for a mixture of turbulence and double diffusion. *J. Phys. Oceanogr.* **37**, 611–624.

Kelley, D. E. 1990 Fluxes through diffusive staircases: a new formulation. *J. Geophys. Res.* **95**, 3365–3371.

Kelley, D. E., Fernando, H. J. S., Gargett, A. E., Tanny, J. & Oezsoy, E. 2003 The diffusive regime of double-diffusive convection. *Prog. Oceanogr.* **56**, 461–481.

Kerstein, A. R. 1991 Linear-eddy modelling of turbulent transport. Part 6. Microstructure of diffusive scalar mixing fields. *J. Fluid Mech.* **231**, 361–394.

Kerstein, A. R. 1999*a* One-dimensional turbulence: model formulation and application to homogeneous turbulence, shear flows, and buoyant stratified flows. *J. Fluid Mech.* **392**, 277–334.

Kerstein, A. R. 1999*b* One-dimensional turbulence. Part 2. Staircases in double-diffusive convection. *Dyn. Atmos. Oceans* **30**, 25–46.

Kerstein, A. R. 2007 BasicODT. Available at: http://groups.google.com/group/odt-research/.

Kerstein, A. R. 2009 One-dimensional turbulence: stochastic simulation of multi-scale dynamics. *Lect. Notes Phys.* **756**, 291–337.

Kerstein, A. R., Ashurst, W. T., Wunsch, S. & Nilsen, V. 2001 One-dimensional turbulence: vector formulation and application to free shear flows. *J. Fluid Mech.* **447**, 85–109.

Kerstein, A. R. & Wunsch, S. 2006 Simulation of a stably stratified atmospheric boundary layer using one-dimensional turbulence. *Bound.-Layer Meteorol.* **118**, 325–356.

Krishnamoorthy, N. 2008 Reaction models and reaction state parametrization for turbulent nonpremixed combustion. PhD thesis, University of Utah.

Larson, N. G. & Gregg, M. C. 1983 Turbulent dissipation and shear in thermohaline intrusions. *Nature* **306**, 26–32.

Law, A. M. & Kelton, W. D. 2000 *Simulation Modeling and Analysis*. McGraw-Hill.

Linden, P. F. 1971 Salt fingers in the presence of grid-generated turbulence. *J. Fluid Mech.* **49**, 611–624.

Linden, P. F. 1974 A note on the transport across a diffusive interface. *Deep Sea Res.* **21**, 283–287.

Linden, P. F. & Shirtcliffe, T. G. L. 1978 The diffusive interface in double-diffusive convection. *J. Fluid Mech.* **87**, 417–432.

Marmorino, G. O. & Caldwell, D. R. 1976 Heat and salt transport through a diffusive thermohaline interface. *Deep Sea Res.* **23**, 59–67.

McDermott, R. J. 2005 Toward one-dimensional turbulence subgrid closure for large-eddy simulation. PhD thesis, University of Utah.

McDougall, T. J. 1981 Double-diffusive convection with a nonlinear equation of state. Part II. Laboratory experiments and their interpretation. *Prog. Oceanogr.* **10**, 91–121.

Merryfield, W. J. 1995 Hydrodynamics of semiconvection. *Astrophys. J.* **444**, 318–337.

Newell, T. A. 1984 Characteristics of a double-diffusive interface at high density stability ratios. *J. Fluid Mech.* **149**, 385–401.

Padman, L. 1994 Momentum fluxes through sheared oceanic thermohaline steps. *J. Geophys. Res.* **99**, 22491–22499.

Padman, L. & Dillon, T. M. 1991 Turbulent mixing near the Yermak Plateau during the coordinated Eastern Arctic experiment. *J. Geophys. Res.* **96**, 4769–4782.

Paparella, F., Spiegel, E. A. & Talon, S. 2002 Shear and mixing in oscillatory doubly diffusive convection. *Geophys. Astrophys. Fluid Dyn.* **96**, 271–289.

Ricks, A. J., Hewson, J. C., Kerstein, A. R., Gore, J. P., Tieszen, S. R. & Ashurst, W. T. 2010 A spatially developing one-dimensional turbulence study of soot and enthalpy evolution in meter-scale buoyant turbulent flames. *Combust. Sci. Technol.* **182**, 60–101.

Schmidt, R. C., Kerstein, A. R., Wunsch, S. & Nilsen, V. 2003 Near-wall LES closure based on one-dimensional turbulence modeling. *J. Comput. Phys.* **186**, 317–355.

Shirtcliffe, T. G. L. 1973 Transport and profile measurements of the diffusive interface in double diffusive convection with similar diffusivities. *J. Fluid Mech.* **57**, 27–43.

Siggia, E. D. 1994 High Rayleigh number convection. *Annu. Rev. Fluid Mech.* **26**, 137–168.

St. Laurent, L. S. & Schmitt, R. W. 1999 The contribution of salt fingers to vertical mixing in the North Atlantic Tracer Release Experiment. *J. Phys. Oceanogr.* **29**, 1404–1424.

Stern, M. E. 1982 Inequalities and variational principles in double-diffusive turbulence. *J. Fluid Mech.* **114**, 105–121.

Suárez, F., Tyler, S. W. & Childress, A. E. 2010 A fully coupled, transient double-diffusive convective model for salt-gradient solar ponds. *Intl J. Heat Mass Transfer* **53**, 1718–1730.

Takao, S. & Narusawa, U. 1980 An experimental study of heat and mass transfer across a diffusive interface. *Intl J. Heat Mass Transfer* **23**, 1283–1285.

Turner, J. S. 1965 The coupled turbulent transports of salt and heat across a sharp density interface. *Intl J. Heat Mass Transfer* **8**, 759–760.

Turner, J. S. 1974 Double-diffusive phenomena. *Annu. Rev. Fluid Mech.* **6**, 37–54.

Turner, J. S. 1979 *Buoyancy Effects in Fluids*. Cambridge University Press.

Worster, M. G. 2004 Time-dependent fluxes across double-diffusive interfaces. *J. Fluid Mech.* **505**, 287–307.

Wunsch, S. & Kerstein, A. R. 2001 A model for layer formation in stably stratified turbulence. *Phys. Fluids* **13**, 702–712.

Wunsch, S. & Kerstein, A. R. 2005 A stochastic model for high-Rayleigh-number convection. *J. Fluid Mech.* **528**, 173–205.